MIT Open Access Articles

Dynamically Tagged Groups of Very Metal-poor Halo Stars from the HK and Hamburg/ESO Surveys

Massachusetts Institute of Technology

Dynamically Tagged Groups of Very Metal-poor Halo Stars from the HK and Hamburg/ESO Surveys

Guilherme Limberg[1] , Silvia Rossi[1] , Timothy C. Beers[2] , Hélio D. Perottoni[1] , Angeles Pérez-Villegas[1,3] ,
Rafael M. Santucci[4,5] , Yuri Abuchaim[1] , Vinicius M. Placco[6] , Young Sun Lee[7] , Norbert Christlieb[8] , John E. Norris[9] ,
Michael S. Bessell[9] , Sean G. Ryan[10] , Ronald Wilhelm[11] , Jaehyon Rhee[12] , and Anna Frebel[13]

[1] Universidade de São Paulo, Instituto de Astronomia, Geofísica e Ciências Atmosféricas, Departamento de Astronomia, SP 05508-090, São Paulo, Brazil
guilherme.limberg@usp.br
[2] Department of Physics and JINA Center for the Evolution of the Elements, University of Notre Dame, Notre Dame, IN 46556, USA
[3] Instituto de Astronomía, Universidad Nacional Autonóma de México, Apartado Postal 106, C.P. 22800, Ensenada, Baja California, Mexico
[4] Universidade Federal de Goiás, Instituto de Estudos Socioambientais, Planetário, Goiânia, GO 74055-140, Brazil
[5] Universidade Federal de Goiás, Instituto de Física, Goiânia, GO 74001-970, Brazil
[6] NSF's National Optical-Infrared Astronomy Research Laboratory, Tucson, AZ 85719, USA
[7] Department of Astronomy and Space Science, Chungnam National University, Daejeon 34134, Republic of Korea
[8] Zentrum für Astronomie der Universität Heidelberg, Landessternwarte, Königstuhl, D-69117 Heidelberg, Germany
[9] Research School of Astronomy and Astrophysics, Australian National University, Canberra, ACT 2611, Australia
[10] School of Physics, Astronomy and Mathematics, University of Hertfordshire, College Lane, Hatfield AL10 9AB, UK
[11] Department of Physics and Astronomy, University of Kentucky, Lexington, KY 40506, USA
[12] Center for Astrophysics | Harvard & Smithsonian, 60 Garden Street, MS-09, Cambridge, MA 02138, USA
[13] Department of Physics and Kavli Institute for Astrophysics and Space Research, Massachusetts Institute of Technology, Cambridge, MA 02139, USA

Abstract

We analyze the dynamical properties of ∼1500 very metal-poor (VMP; [Fe/H] $\lesssim$ −2.0) halo stars, based primarily on medium-resolution spectroscopic data from the HK and Hamburg/ESO surveys. These data, collected over the past 30 yr, are supplemented by a number of calibration stars and other small samples, along with astrometric information from Gaia DR2. We apply a clustering algorithm to the 4D energy-action space of the sample, and identify a set of 38 dynamically tagged groups (DTGs), containing between 5 and 30 member stars. Many of these DTGs can be associated with previously known prominent substructures such as Gaia-Sausage/Enceladus (GSE), Sequoia, Helmi Stream (HStr), and Thamnos. Others are associated with previously identified smaller dynamical groups of stars and streams. We identify 10 new DTGs as well, many of which have strongly retrograde orbits. We also investigate possible connections between our DTGs and ∼300 individual r-process-enhanced (RPE) stars from a recent literature compilation. We find that several of these objects have similar dynamical properties to GSE (5), the HStr (4), Sequoia (1), and Rg5 (1), indicating that their progenitors might have been important sources of RPE stars in the Galaxy. Additionally, a number of our newly identified DTGs are shown to be associated with at least two RPE stars each (DTG-2: 3, DTG-7: 2; DTG-27: 2). Taken as a whole, these results are consistent with ultra-faint and/or dwarf spheroidal galaxies as birth environments in which r-process nucleosynthesis took place, and then were disrupted by the Milky Way.

Unified Astronomy Thesaurus concepts: Milky Way dynamics (1051); Milky Way evolution (1052); R-process (1324); Population II stars (1284); Milky Way stellar halo (1060)

Supporting material: machine-readable tables

1. Introduction

The currently accepted model for the formation of the Galactic stellar halo (hereafter "halo") consists of frequent mergers between the nascent Milky Way (MW) and dwarf satellite galaxies of various masses, based on early suggestions from Searle & Zinn (1978), and numerous efforts since. This bottom-up scenario is supported by theoretical predictions from the Λ cold dark matter cosmological paradigm (Spergel et al. 2007), and numerical simulations of increasing sophistication based on it (see, e.g., Somerville & Davé 2015).

The discovery of the Sagittarius dwarf spheroidal, a galaxy in the process of tidal disruption (Ibata et al. 1994), and smaller stellar streams in the halo (e.g., Helmi et al. 1999; Chiba & Beers 2000) provided strong evidence for this assembly mechanism. Metallicities ([Fe/H][14]), radial velocities (RVs), and proper

motions made available by large surveys such as the Sloan Digital Sky Survey (SDSS; York et al. 2000), in particular its stellar-specific sub-survey Sloan Extension for Galactic Exploration and Understanding (SEGUE; Yanny et al. 2009), led to the proposition (supported by many studies since) that the halo comprises at least two overlapping stellar populations, the inner-halo population (IHP) and the outer-halo population (OHP), with differences in their spatial density distributions, stellar kinematics, and chemical abundances (Carollo et al. 2007, 2010; de Jong et al. 2010; Beers et al. 2012; An et al. 2013, 2015; Lee et al. 2017, 2019; Kim et al. 2019; An & Beers 2020).

Even limited kinematic information has been used to infer the presence of substructures throughout the halo of the MW. For example, Schlaufman et al. (2009, 2011, 2012) used RVs alone to identify a plethora of elements of cold halo substructures within the inner-halo region from the SDSS/SEGUE surveys. An et al. (2013, 2015) combined proper motions with photometric metallicities to estimate the fractions of IHP and OHP stars in

---

[14] Definition of abundance of a star (⋆) relative to the Sun (⊙): $[A/B] = \log(N_A/N_B)_\star - \log(N_A/N_B)_\odot$, where N_A (N_B) are the number densities of atoms for elements A (B).

the local neighborhood. An & Beers (2020) used the powerful combination of photometric metallicities and precision astrometric surveys to produce a "blueprint" of the known stellar populations in the disk and halo systems of the Galaxy. In the process, these authors confirmed the presence of a dynamically heated disk population, named the "splashed disk" (SD; Bonaca et al. 2017; Di Matteo et al. 2019; Amarante et al. 2020a, 2020b; Belokurov et al. 2020), and demonstrated that the metal-weak thick disk (MWTD) is an independent structure from the canonical thick disk (see also Carollo et al. 2019).

Many recent works have used full space motions, based on RVs and astrometry (parallaxes and proper motions) provided by Gaia's Data Releases (DRs; Gaia Collaboration et al. 2016a, 2016b, 2018a), combined with previously available spectroscopic and photometric data, to analyze the kinematics and abundances for very large samples of halo and disk stars (see Helmi 2020 for a review). It has been proposed that the IHP is dominated by the remnant of a single, relatively massive (stellar mass $M_\star \sim 6 \times 10^8 M_\odot$) merger event, approximately 10 Gyr ago, named the Gaia-Sausage (Belokurov et al. 2018; Haywood et al. 2018; Myeong et al. 2018b) or Gaia-Enceladus (Helmi et al. 2018). Orbital modeling indicates that stars in this system present highly radial orbits (a signature noted very early on by, e.g., Norris 1986; Sommer-Larsen et al. 1997; Chiba & Beers 2000; Ryan & Smith 2003). In an independent effort, Helmi et al. (2018) investigated the properties of this substructure, and were able to associate it with one of the two distinct main-sequence turnoffs identified in the local halo (Gaia Collaboration et al. 2018b).

In a series of papers, Myeong et al. (2018c, 2018d, 2019) argued that a population of high orbital energy (hereafter "energy"; E), retrograde halo stars partially overlaps with Gaia-Enceladus, differentiating this proposed event from the one described by Belokurov et al. (2018). Indeed, Myeong et al. (2019) suggested that a different substantial progenitor could be attributed to this substructure, the Sequoia galaxy ($M_\star \sim 5 \times 10^7 M_\odot$), providing the bulk of the high-energy, retrograde outer-halo stars. On the other hand, Koppelman et al. (2019a) attributed the low-energy counterpart of Sequoia to a different merging event of smaller scale, named Thamnos ($M_\star \sim 5 \times 10^6 M_\odot$), previously reported in part by Helmi et al. (2017) and Koppelman et al. (2018). Stars linked to this system also have higher values of both [Mg/Fe] and [Al/Fe], thus suggesting a chemical separation from Sequoia as well. In contrast to Gaia-Sausage/Enceladus (GSE), Thamnos exhibits lower values of [Fe/H], consistent with the progenitor being a smaller galaxy.

All of the above efforts have contributed greatly to our current understanding of the complex formation history of the Galactic halo, focusing on identifying its most prominent substructures. However, low-mass dwarf galaxies accreted by the MW and disrupted into the halo would not be expected to present strong spatial over-densities (streams), in particular in the low stellar-density outer-halo region. For the purpose of finding the remnants of such systems, one would consequently want to construct samples of stars with similar characteristics to their parent mini-halos' stellar populations, increasing the fraction of objects that originated in these environments (see Simon 2019 for a review).

Since low-mass dwarf satellite galaxies primarily host very metal-poor (VMP; [Fe/H] < −2.0) stars, Yuan et al. (2020b) proposed the examination of stellar samples of VMP stars in order to identify their debris in the local halo. These authors applied a neural-network-based technique to dynamically cluster their sample of ∼3000 stars (from LAMOST DR3; Li et al. 2018, with re-determined stellar parameters by Beers) in energy and angular-momentum space. They found 57 dynamically tagged groups (DTGs), many of them related to larger substructures, such as GSE, and some groups from Myeong et al. (2018d). They were also able to associate previously known chemically peculiar (r-process-enhanced or carbon-enhanced) stars with them. The pioneering effort of Roederer et al. (2018) identified eight dynamical groups of r-process-enhanced (RPE) stars (with three or four stars each) from a relatively small sample of 35 such objects. Chemo-dynamically tagged groups have been identified from much larger samples of RPE and carbon-enhanced metal-poor (CEMP; [C/Fe] > +0.7 and [Fe/H] < −1.0) stars by Gudin et al. (2020). Furthermore, Yuan et al. (2020a) used metal-poor blue horizontal-branch and RR Lyrae stars to discover a low-mass stellar-debris stream apparently associated with a pair of globular clusters in the outer-halo region, which they named LMS-1. This substructure was independently confirmed by Naidu et al. (2020), which they called Wukong. There are surely many more such small groups/streams that remain to be identified.

VMP substructures recognized from these efforts are possibly remnants of ultra-faint dwarf (UFD) and low- to intermediate-mass dwarf spheroidal (dSph) galaxies that were accreted and shredded by the MW. Since there now exists a plentiful supply of VMP stars that are much closer (and hence brighter) than individual stars in any surviving dwarf satellite, these objects provide an opportunity to study the chemical-evolution histories of their now-disrupted parent systems in much greater detail. This possibility is particularly appealing in the context of the recent discoveries of RPE stars in the UFD galaxies Reticulum II (Ji et al. 2016; Roederer et al. 2016) and Tucana III (Hansen et al. 2017; Marshall et al. 2019). Classical dSph galaxies might also present moderately enhanced (r-I; +0.3 < [Eu/Fe] ⩽ +0.7) and highly enhanced (r-II; [Eu/Fe] > +0.7)[15] RPE stars.

The fundamental goal of this paper is to identify additional fragments of dwarf satellites that have been merged with the Galactic halo. We also investigate possible associations of such systems with the large sample of RPE stars compiled by Gudin et al. (2020). We establish a straightforward, easily reproducible framework to identify DTGs, and apply it to the combined sample of some 1500 VMP stars (with available estimates of metallicity, RVs, and astrometric data, after removal of possible non-halo stars and stars with uncertain distance estimates) originally identified in the HK survey of Beers and colleagues and the Hamburg/ESO (HES) survey of Christlieb and collaborators, along with a number of calibration stars and halo star candidates with spectroscopic data taken during the HK/HES surveys (see Figure 1). The most interesting of these DTGs will provide the opportunity to explore the nucleosynthetic processes operating in the environments of UFD and/or dSph galaxies in the past.

This paper is organized as follows. Section 2 describes the assembly of our VMP sample, including estimates of their stellar atmospheric parameters, as well as their kinematic and astrometric data. Section 3 reports our calculations of the dynamical properties for the stars in this sample. Section 4 describes our substructure search methodology, and the assignment of individual stars into 38 DTGs. Our analysis of

---

[15] We adopt the definitions for r-process enrichment from Holmbeck et al. (2020).
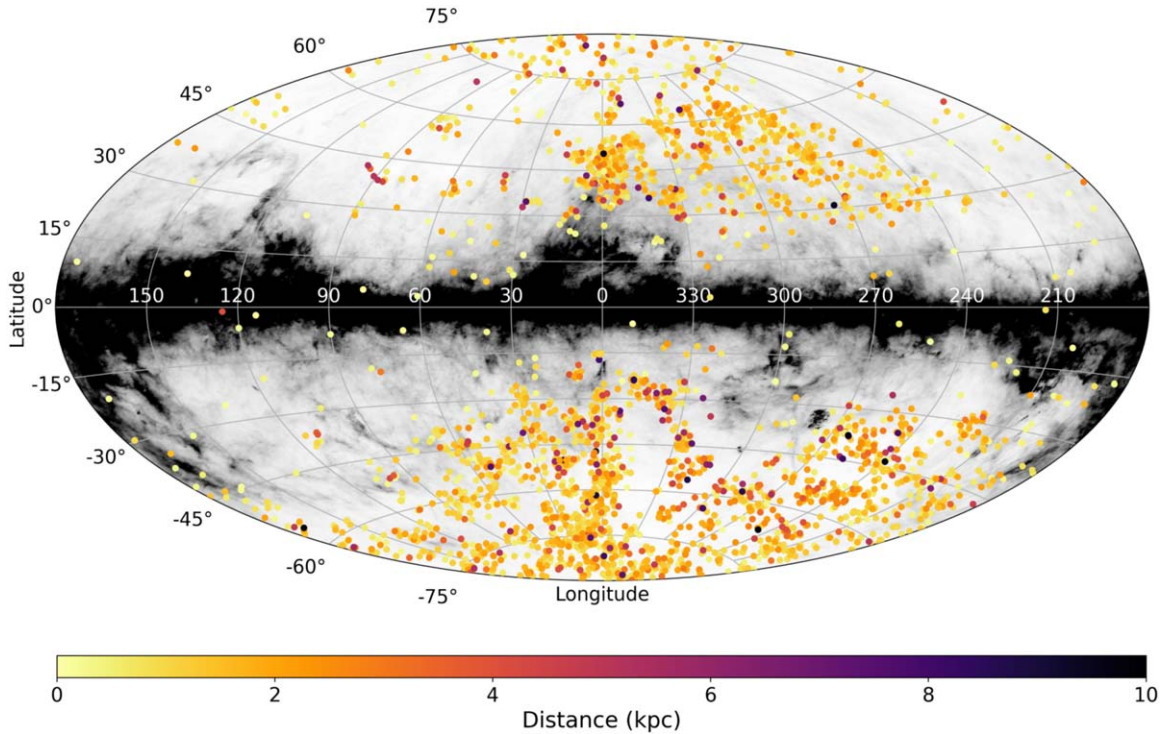
Figure 1. Distribution of the VMP HK/HES sample in the Galactic coordinate system, color-coded by heliocentric distances (see the text) with relative errors smaller than 20% of the nominal values (Section 2). The background all-sky distribution of the Galactic reddening comes from the Schlegel et al. (1998) map, as re-calibrated by Schlafly & Finkbeiner (2011). The different gray scales represent $E(B - V)$ values from 0.0 (white) to 0.5 (black).

these DTGs is presented in Sections 5 and 6, including their possible associations with previously recognized substructures and dynamical groups. In Section 7, we map previously known RPE stars onto our DTGs. Finally, Section 8 provides concluding remarks and a brief discussion.

2. Data

2.1. The HK/HES Spectra

Beginning almost fifty years ago with the pioneering work of Bond (1970, 1980) and Bidelman & MacConnell (1973), photographic objective-prism techniques have proven to be efficient sieves for identifying large numbers of stars that are metal deficient (and/or chemically peculiar). These efforts were expanded by the HK survey[16] (Beers et al. 1985, 1992), and later by the HES survey (Christlieb et al. 2008), which included fainter stars, making it possible to explore deeper into the Galactic halo, where more metal-poor stars have been found. Both surveys sought to identify such stars via visual (HK) or automated (HES) inspection of the prism plates, searching for stars with weak, or absent, Ca II K lines in their very low-resolution ($R = \lambda/\Delta\lambda \sim 300$) spectra.

Over the past three decades, the metal-poor candidates identified in these surveys have been followed-up with medium-resolution ($1200 \lesssim R \lesssim 2000$) spectroscopy with a wide variety of telescopes and instruments. The typical spectral coverage of these spectra are 3500–5000 Å, although there was wide variation. The decisions as to which targets to observe are difficult to quantify, since many observers contributed to these efforts. In addition, in some cases, photometric information

from independent efforts (HK), or taken directly from an approximate calibration of the prism spectra (HES), were obtained in advance of the spectroscopic follow-up. A complete description of the HK and HES candidate selection can be found in Beers et al. (1985, 1992) and Christlieb et al. (2008), respectively.

Metallicity ([Fe/H]) estimates were originally obtained by application of a number of techniques, initially based solely on the indices tracking the equivalent width of the Ca II K line, as a function of measured or estimated color (often $B - V$; see Beers et al. 1990b). Later, techniques designed to obtain estimates of the carbonicity ([C/Fe]), based on the strength of the CH G-band feature at ∼4330 Å, were developed (see, e.g., Rossi et al. 2005; Placco et al. 2010, 2011, and references therein). Further refinements, including approaches to avoid difficulties involving the saturation of Ca II K indexes at higher metallicities and/or lower temperatures were incorporated (see, e.g., Beers et al. 1999; Rossi et al. 2005). Many of these same techniques were used as the starting point for more modern pipelines used for similar medium-resolution spectra from SDSS (Lee et al. 2008a, 2008b) and LAMOST (Xiang et al. 2015).

One of the primary drivers for these endeavors was to develop lists of vetted VMP stars that served as input targets for large-scale high-resolution spectroscopic follow-up campaigns involving astronomers worldwide (e.g., the "Extremely Metal-poor Stars" program of Norris et al., e.g., Norris et al. 1996; the "First Stars" program of Cayrel et al., e.g., Hill et al. 2002; Cayrel et al. 2004; the CEMP stars follow-up program by Aoki et al., e.g., Aoki et al. 2007; the "Zero-Z" program of Cohen et al., e.g., Cohen et al. 2008). For almost two decades, the HK/HES surveys were responsible for the discovery of the majority of stars known with [Fe/H] < −3.0 (see Frebel et al. 2006; Placco et al. 2011; Roederer et al. 2014), including the

---

[16] The first observations on this program were made in the late 1970s by George Preston and Stephen Shectman; hence, in the early literature, this survey is sometimes referred to as the "Preston-Shectman" survey.

first hyper metal-poor ([Fe/H] < −5.0) stars found in the Galactic halo (Christlieb et al. 2002; Frebel et al. 2005).

2.2. Reanalysis of the HK/HES Spectra

As the determinations of [Fe/H] (and [C/Fe]) for the HK/HES medium-resolution spectra were acquired over many years (some including photometric information, some not), with a variety of instruments and calibrations, for our present purpose, it is necessary to perform a homogeneous re-analysis. Of course, we now have available multiple new techniques, photometry, and high-resolution calibrations that can be brought to bear on this effort.

All estimates of stellar atmospheric parameters for our stars have been obtained by application of the n-SSPP pipeline (Beers et al. 2014, 2017), a modified version of the SEGUE Stellar Parameter Pipeline (SSPP; Lee et al. 2008a, 2008b, 2011, 2013). The n-SSPP is a compilation of routines that utilizes spectroscopic and photometric inputs to perform various estimates of the stellar parameters. It employs χ^2 minimization between the analyzed spectra and a dense grid of synthetic ones, as well as other techniques, where suitable, depending on the wavelength coverage of the input. Then, the best set of values is adopted. See also Placco et al. (2018, 2019) for recent applications of these methods to low-metallicity stars observed with a variety of instruments. The errors for effective temperatures ($T_{\rm eff}$) and surface gravity ($\log g$) values are ± 150 K and ± 0.35 dex, respectively. The adopted solar abundances are from Asplund et al. (2009). The typical uncertainty for estimates of [Fe/H] and [C/Fe] is ± 0.15–0.25 dex, depending on $T_{\rm eff}$ and signal-to-noise ratio. Comparisons between the metallicity and carbonicity values from the n-SSPP and those from high-resolution spectroscopy are published in Placco et al. (2014a); they are quite compatible (at the 1σ level).

The RVs have been measured with the line-by-line and cross-correlation techniques (Beers et al. 1999, 2014, 2017) and are precise to 10–15 km s^{-1}. Figure 2 shows the comparison between our measured RVs and those from Gaia DR2 (when available). The shaded areas represent the 1σ and 2σ ranges, where σ is the biweight scale (Beers et al. 1990a). This metric is more suitable, since the distribution of residuals is affected by occasional outliers. Many of the larger differences are likely due to the presence of binary systems or problems with the wavelength calibration of the medium-resolution spectra for individual stars. We remove any stars residing outside this 2σ region from our analysis, whenever Gaia RVs are available for comparison. Even though other sources of RVs are usable for part (∼20%) of our sample, we have decided to retain these directly measured values in order to preserve the homogeneity of our uncertainties, and avoid introducing unnecessary biases.

2.3. The VMP HK/HES Sample

To construct our initial sample, we first remove apparent white dwarfs or other warm objects, such as subdwarf B stars, spectra with clear Ca II K-line core emission features, or spectral defects in the wavelength region of the Ca II K/H lines (3900 Å–4000 Å). For objects with more than a single observation, we adopt the median of the estimated metallicities. We then exclude anything bluer than the main-sequence turnoff by limiting our sample to $T_{\rm eff} < 7000$ K. Note that this temperature cutoff still includes a number of halo blue stragglers and horizontal-branch stars. Finally, we have selected objects with [Fe/H] ⩽ −1.8, as these will include VMP stars within the expected error bars on the
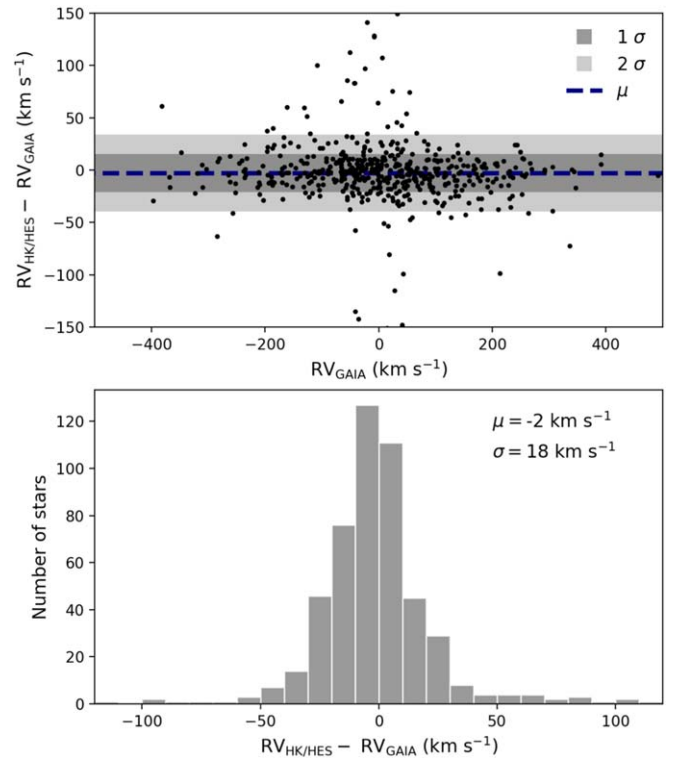

Figure 2. Upper panel: residuals between measured (line-by-line or cross-correlation) RVs of the VMP HK/HES sample and those from Gaia DR2. The shaded areas represent the 1σ and 2σ ranges, where σ is the biweight scale. The dashed blue line represents the biweight central location (μ). Lower panel: histogram of the residuals.

metallicity estimates. We refer to all of these stars below as VMP stars. This results in a total initial sample of 4443 VMP stars.

Note that the initial sample includes a small fraction (∼15%) of stars—primarily used for parameter calibration and/or short lists of candidate halo stars from other samples—that were observed with the same resolving power and wavelength coverage as the HK/HES stars during the course of the main follow-up effort (see Figure 3). These other small samples include data from: (i) Beers et al. (2001), comprising cooler stars from the Edinburgh-Cape Blue Object Survey (indicated by the prefix "EC" in our sample); (ii) Beers et al. (2002), comprising candidate metal-poor stars identified close to the Galactic plane in the Luminous Stars Extension survey (identified with the prefix "LSE" in our sample); (iii) Rhee (2001), comprising metal-poor candidates (primarily cooler giants) identified from digital scans of the HK survey plates with the Automatic Plate Machine facility in Cambridge, UK (Rhee et al. 1999), known as the HK II survey (identified with the prefix "II" in our sample); (iv) Frebel et al. (2006; see also Beers et al. 2017), comprising bright metal-poor candidates from the HES plates; and (v) Beers et al. (2014), comprising metal-poor candidates selected by Bidelman & MacConnell (1973; see also Norris et al. 1985). For simplicity of notation, we refer to the full sample as the VMP HK/HES sample (listed in Appendix A.1; Table 5).

We cross-match the VMP HK/HES sample with Gaia DR2 to obtain accurate proper motions, where available. We combine these data with distances from Anders et al. (2019), estimated with the StarHorse code (Queiroz et al. 2018, 2020) in a Bayesian framework. The 50th percentile of these distance distributions are
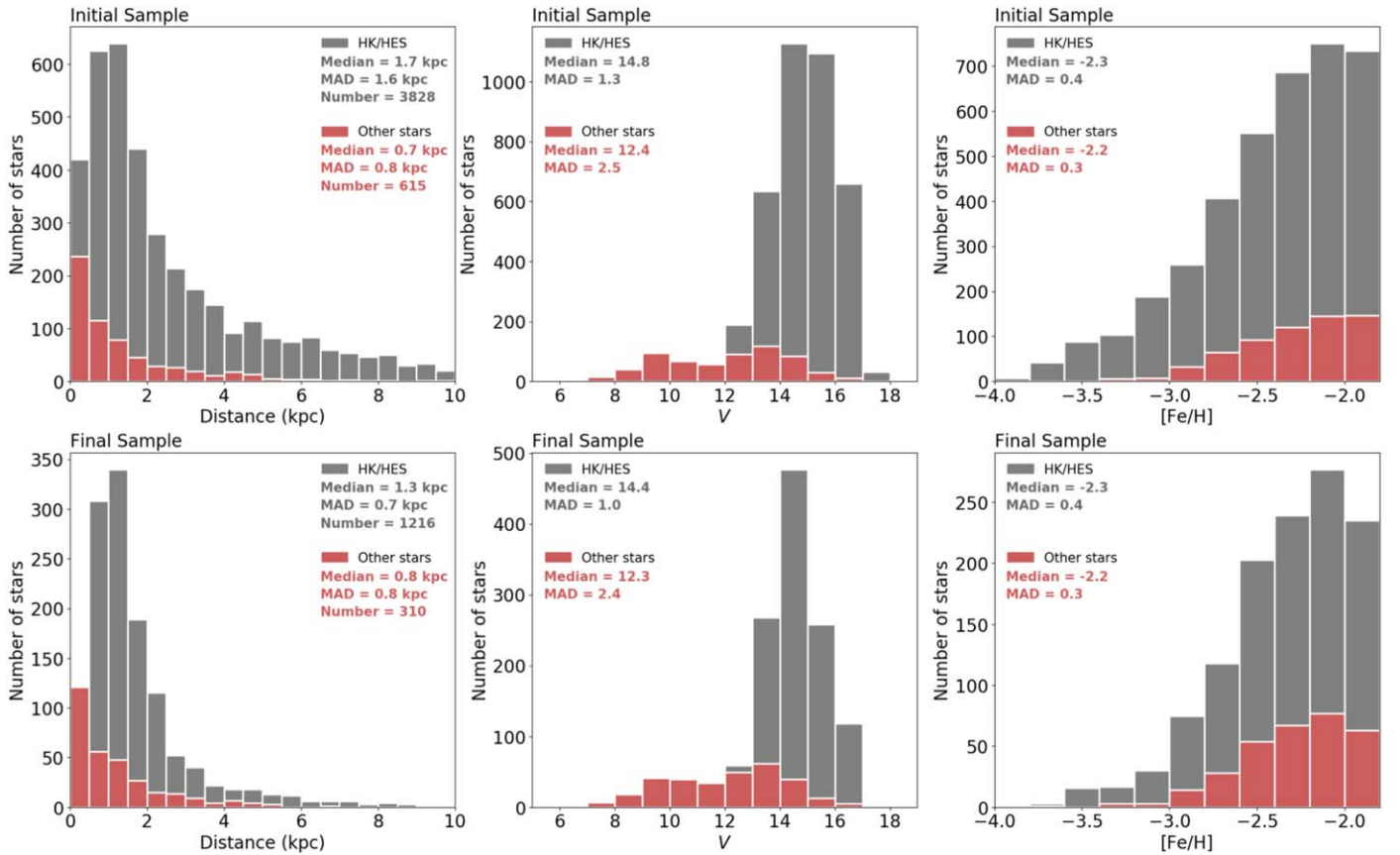
Figure 3. Histograms of the distributions of heliocentric distances, V-band magnitudes, and [Fe/H] for both the initial sample (upper row) and the final sample (lower row), as described in Section 2. Gray bars represent the VMP HK/HES stars. Red bars represent stars from other sources, including many calibration stars, as discussed in Section 2.3. Medians and median absolute deviation (MAD) values have been listed following the color scheme of the histograms. The total number of stars of each sample has been added in the left panels.

compatible with the inverse of the Gaia parallaxes within 2–3 kpc from the Sun, but can be used when the reported Gaia parallax is either negative or missing. Finally, we have restricted our sample to stars with relative distance errors smaller than 20% of their nominal values, assuming Gaussian distributions according to its 16th and 84th percentiles. This cut yields heliocentric distances $\lesssim 5$ kpc (Figure 3), with few exceptions. Out of these stars, the vast majority ($\sim$97%) have re-normalized unit weight errors within the recommended interval (RUWE < 1.4; Lindegren et al. 2018), which can be used to obtain reliable dynamical-parameter estimates.

We have adopted a velocity of the local standard of rest (LSR) of $V_{\rm LSR} = 232.8$ km s^{-1} (McMillan 2017), and a peculiar motion of the Sun with respect to the LSR of $(U,V,W)_\odot = (11.1, 12.24, 7.25)$ km s^{-1} (Schönrich et al. 2010). Then, the position on the sky, distance, proper motions, and RVs of the stars are converted to the Cartesian Galactic phase-space positions and velocities using `Astropy` Python tools (Astropy Collaboration et al. 2013, 2018). Finally, we have made a cut in velocity, $|V - V_{\rm LSR}| > 210$ km s^{-1}, to primarily retain stars from the halo. Applying this criterion leaves a final sample of 1540 likely VMP HK/HES halo stars with data suitable for dynamical analysis (these are listed, along with the adopted dynamical parameters, in Appendix A.2; Table 6).

2.4. The RPE Stars Sample

For the mapping of RPE stars onto our DTGs, carried out in Section 7, we have adopted the recent compilation of r-I and r-II stars from Gudin et al. (2020). The majority of these objects come from the *R*-Process Alliance data releases (Hansen et al. 2018; Sakari et al. 2018; Ezzeddine et al. 2020; Holmbeck et al. 2020), complemented with additional data from JINAbase (Abohalima & Frebel 2018). These stars are all metal-poor ([Fe/H] < -1.0) and at least moderately enriched in r-process elements ([Eu/Fe] $> +0.3$; [Ba/Eu] $<$ 0.0). We do not apply the [Fe/H] $\leqslant -1.8$ cut since these stars are already chemically peculiar, independently of their metallicities. For consistency, we have used the same kinematic criteria described in Section 2.3, but keeping stars with relative distance errors up to 30%, which avoids constraining our sample too much. These larger errors in distances lead to increasing uncertainties in the dynamical parameters. However, since we employ a statistical method for the cluster assignment, such errors will propagate into smaller membership probabilities, which we independently evaluate (Section 4). Our more rigorous selection yielded a total sample of 305 RPE stars for dynamical analyses.

3. Dynamical Properties

Estimated dynamical parameters for the VMP HK/HES (and RPE) sample have been obtained adopting the axisymmetric Galactic potential of McMillan (2017). This Galactic model includes stellar thin and thick disks, gaseous disks, a flattened bulge, and spherical dark matter halo. In this model, the corresponding distance from the Sun to the Galactic center is $R_\odot = 8.2$ kpc (Bland-Hawthorn & Gerhard 2016; Gravity Collaboration et al. 2019).

Stellar orbits have been integrated with the publicly available library `AGAMA` (Vasiliev 2019) to obtain estimates of the apocentric distance ($r_{\rm apo}$), pericentric distance ($r_{\rm peri}$), and eccentricity ($e = (r_{\rm apo} - r_{\rm peri})/(r_{\rm apo} + r_{\rm peri})$) for each star (Figure 4). Energies (E) and actions (J_R, J_ϕ, J_z; cylindrical coordinates) have also been computed with `AGAMA`, which implements the numerical method outlined by Binney (2012). The actions[17] can be interpreted as follows. The radial action ($J_R \in [0, \infty]$) is related to a star's orbital eccentricity, as it captures the extent of its radial excursion. The azimuthal action ($J_\phi \in [-\infty, \infty]$) represents the stars' rotation around the Galactic center. Stars with $J_\phi > 0$ are in prograde motion. The vertical action ($J_z \in [0, \infty]$) can be interpreted as the extent of the vertical excursion of a star's orbit relative to the Galactic plane. We have performed 1000 Monte Carlo realizations for each star, taking into account uncertainties in the heliocentric distances, proper motions, and RVs, in order to assess their effect on the derived parameters.

The medians of the distributions of each dynamical quantity from the Monte Carlo realizations have been adopted as our nominal values. We have removed 14 stars presenting orbits that are formally unbound to the Galaxy ($E > 0$). Our final sample for the substructure search comprises 1526 unique VMP stars with atmospheric parameters, six-dimensional phase-space vectors, energies, actions, and other dynamical quantities. The median metallicity of this final selected sample is [Fe/H] = -2.3, and its median absolute deviation (MAD) is 0.4 dex (Figure 3).

Figure 4 shows histograms of the pericentric distances, $r_{\rm peri}$, apocentric distances, $r_{\rm apo}$, and the maximum distance from the Galactic plane achieved during the stars' orbits, $Z_{\rm max}$, for the stars in the final sample. From inspection of this figure, the distributions of these quantities for the HK/HES stars and the other stars (mostly calibration stars) are quite similar, justifying our choice to combine them for the clustering analysis.

4. Substructure Search

We seek DTGs in the VMP HK/HES sample in the space defined by the energy and actions (E, J_R, J_ϕ, J_z). These parameters (with slight variations) have been extensively used to search for the dynamical signatures of accreted material in the Galaxy (Helmi et al. 2017; Roederer et al. 2018; Myeong et al. 2018d; Koppelman et al. 2019a; Yuan et al. 2019, 2020a, 2020b; Hansen et al. 2019; Naidu et al. 2020).

4.1. Clustering Method

The identification of DTGs was carried out using the clustering algorithm Hierarchical Density-Based Spatial Clustering of Applications with Noise (`HDBSCAN`;[18] Campello et al. 2015), implemented in Python by McInnes et al. (2017).

`HDBSCAN` has been developed to work with an initially unknown total number of groups, having variable shapes and density contrasts. Another important feature is that `HDBSCAN` is robust in the presence of noisy data; there is no dependence on the underlying assumption of smooth background models in energy-action space that past works relied upon to deal with this challenge. It is also convenient that the fundamental hyperparameter that `HDBSCAN` requires to operate is the minimum
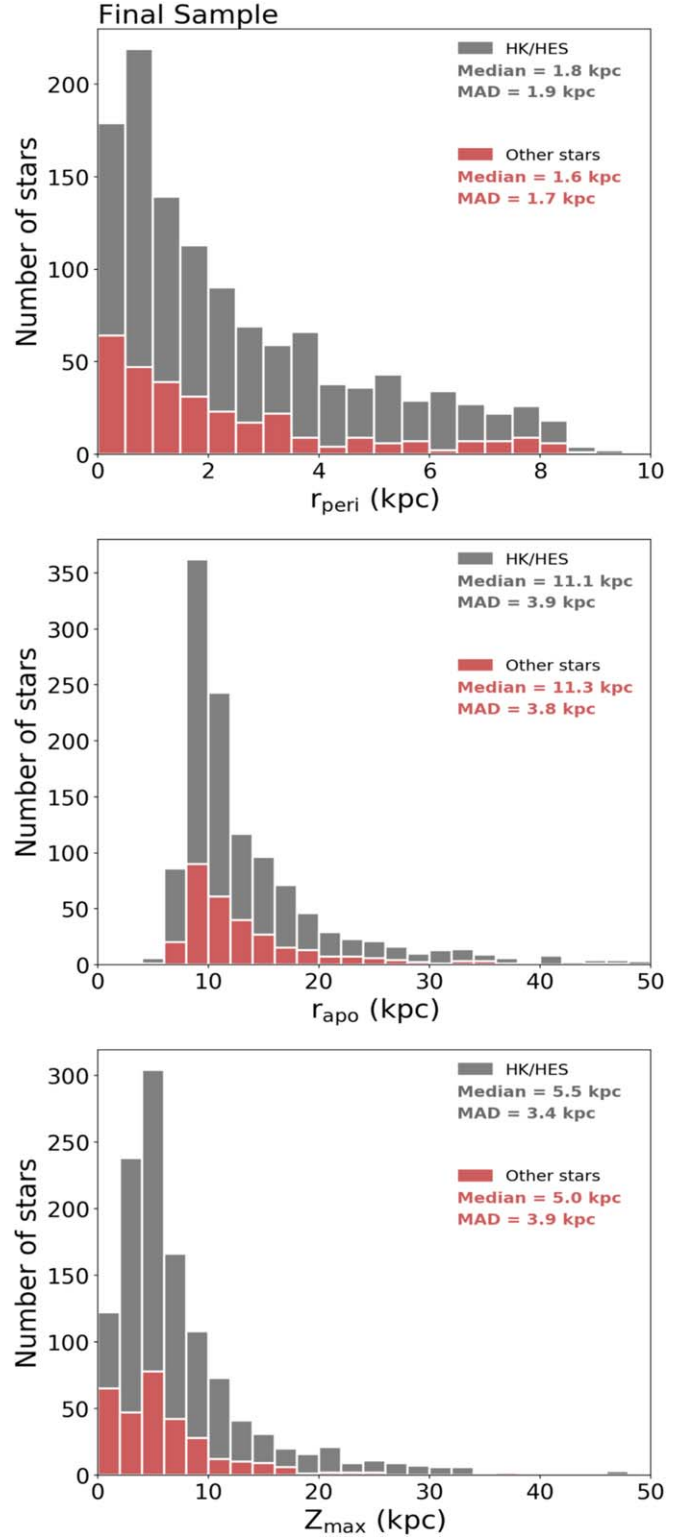
Figure 4. Histograms of the distributions of $r_{\rm peri}$ (top), $r_{\rm apo}$ (middle), and $Z_{\rm max}$ (bottom) for the final sample. Colors are the same as Figure 3. The $r_{\rm peri}$ is presented in 0.5 kpc bins, while the $r_{\rm apo}$ and $Z_{\rm max}$ are divided into 1.0 kpc bins. Medians and median absolute deviation (MAD) values have been listed following the color scheme of the histograms.

number of elements to form a valid group (`min_cluster_size`), which is physically meaningful.

`HDBSCAN` constructs a hierarchical cluster tree based on the estimated local densities for each point in the multidimensional

---

[17] The complete formalism on actions can be found in Section 3.5 of Binney & Tremaine (2008). For a practical interpretation of actions, see Figure 2 of Trick et al. (2019).
[18] https://hdbscan.readthedocs.io

parameter space. Two points are considered connected if they form a dense region in this parameter space. The clusters are likely to be real if they are persistent for different density thresholds, from very low to very high. These can be interpreted as persistent clusters (with a `min_cluster_size`) with less-likely members falling out of them as they move through the hierarchical tree. This exercise ensures that the resulting groups are very stable.

We have chosen `min_cluster_size = 5` and `cluster_selection_method = "leaf"` as input parameters in order to build the cluster hierarchy tree. This choice, in particular the "leaf" mode, is optimized for the detection of fine-grained substructures in favor of larger ones. After testing with the algorithm, we have noticed that the overall behavior of the groups does not change significantly with `min_cluster_size`. Essentially, smaller clumps are erased when this parameter is increased, as expected. Therefore, we have avoided smaller values for the `min_cluster_size`, as that could lead to an unrealistic number of groups. We have also avoided values that are too large, as that would not be in keeping with our objective of finding small groups that could have originated from low-mass systems. The larger substructures in our data can still be mapped out following the execution of the procedure, assembled from the smaller, robust ones (Section 5). This choice is also consistent with the work of both Yuan et al. (2020b) and Myeong et al. (2018a), who accepted groups containing at least four and five members, respectively, making our study comparable to theirs. Again, we note that the clusters are built exclusively from the VMP sample. The RPE stars are mapped onto the groups only after the cluster assignment has already been completed.

Although we expect clusters identified by HDBSCAN to be quite stable, we still need to assess the statistical significance of the groups against variations in the dynamical properties of each member star due to their estimated uncertainties. We have sampled 1000 sets of (E, J_R, J_ϕ, J_z) from the 16th and 84th percentiles of each quantity for each star in a Monte Carlo framework. Then, we throw these perturbed data sets back into the hierarchical tree, and re-evaluate their cluster assignments. An object is considered a valid member of a given group if it was assigned at least 200 times to the same cluster out of the 1000 Monte Carlo realizations. We take this to indicate that the star presents at least a 20% membership probability. We define the confidence level of a given group (see Table 1) as the average membership probability of its member stars.

Application of this method results in the identification of 38 significant DTGs,[19] comprising ~400 stars (27% of the final sample). The characteristics of each DTG are listed in Table 1, and are represented with different symbols in Figure 5. Those with qualitatively similar dynamical properties are shown with similar colors. The number of stars in each dynamical group ranges from 5 to 30. The one with the highest confidence level is DTG-10 (94%). The DTGs with the lowest confidence are DTG-12 and DTG-23, both at 39%. Just over half (23/38; 60%) are retrograde ($\langle J_\phi \rangle < 0$). We compare our results to those from the literature and further discuss the nature of our DTGs in Sections 5 and 6.

---

[19] We follow the nomenclature proposed by Yuan et al. (2020b). Dynamical groups resulting from different analyses can be recognized by the initials of the first author's names, the year of publication, and the number of the DTG. Our DTG-1, for instance, would be referenced as GL20:DTG-1.

Table 1
DTGs in the VMP HK/HES Sample

| DTG	Members	Confidence	Comments
1	9	84%	Sequoia
2	8	87%	Polar, New[a]
3	18	88%	Helmi Stream
4	8	66%	Polar, New
5	10	66%	Sequoia
6	6	80%	Rg5
7	7	50%	Retrograde, New
8	14	56%	ZY20:DTG-35
9	7	58%	Polar, New
10	5	94%	Prograde, New
11	13	67%	GSE
12	6	39%	Retrograde, New
13	6	52%	ZY20:DTG-39
14	11	66%	Retrograde, New
15	6	80%	Prograde, New
16	5	41%	ZY20:DTG-33
17	18	67%	Prograde, New
18	8	63%	ZY20:DTG-33
19	6	51%	Retrograde, New
20	6	57%	GSE
21	8	62%	GSE
22	7	62%	ZY20:DTG-33
23	7	39%	GSE
24	12	62%	GSE
25	10	41%	Thamnos
26	8	59%	Thamnos
27	13	88%	ZY20:DTG-19
28	5	60%	GSE
29	14	66%	GSE
30	20	53%	GSE
31	12	47%	Thamnos
32	13	70%	Thamnos
33	10	45%	Thamnos
34	19	48%	GSE
35	8	57%	GSE
36	21	64%	GSE
37	30	61%	GSE
38	10	62%	GSE

Note.
[a] Tentative association with other reported substructure (Section 6.1).

5. Mapping Larger Substructures

5.1. GSE

The structure known as GSE has been suggested to be the remnant of the last large-scale merging event experienced by the Galaxy (Belokurov et al. 2018; Haywood et al. 2018; Helmi et al. 2018), containing the majority of the accreted stars in the nearby halo. Its members form a well-defined sequence in the color–magnitude diagram presented in Gaia Collaboration et al. (2018b) for stars with halo-like kinematics. They also exhibit typically low metallicities ([Fe/H] $\lesssim -0.7$; Di Matteo et al. 2019) and α-element abundance ratios (Hayes et al. 2018; Mackereth et al. 2019; also noted earlier on by Nissen & Schuster 2010). These stars are distinguishable in velocity space, as they form an extended distribution in v_R (velocity toward the radial direction of the cylindrical coordinate system) around an azimuthal velocity (v_ϕ) close to zero (Koppelman et al. 2018; Feuillet et al. 2020), which translates into highly eccentric orbits (Naidu et al. 2020). Moreover, stars from the GSE progenitor are usually old ($\gtrsim$10 Gyr; Gallart et al. 2019;
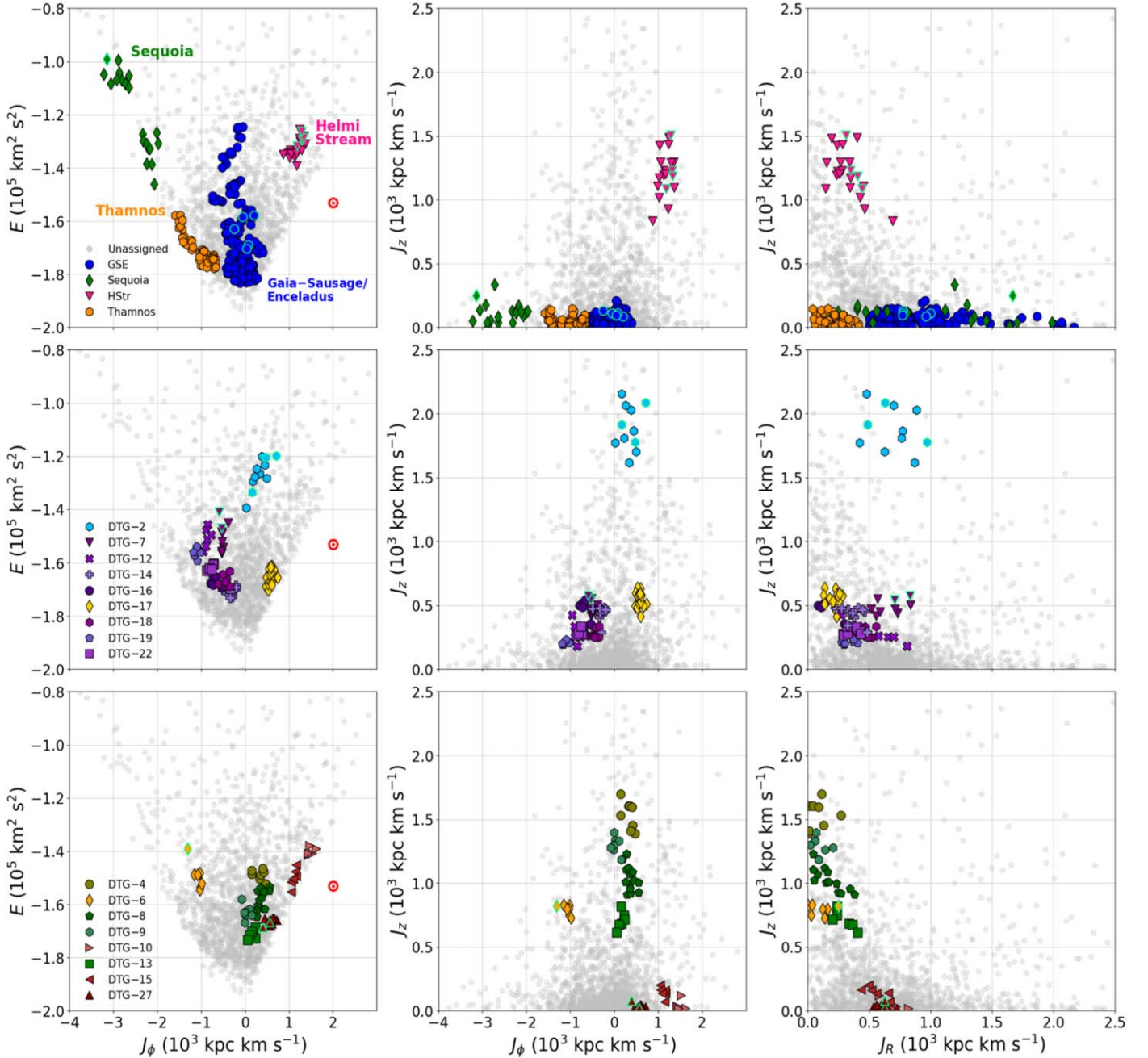
Figure 5. Energy–action-space plots of the VMP HK/HES sample. Left column: (E, J_ϕ). The prograde, low-energy corner of the (E, J_ϕ) diagrams are depopulated due to the $|V - V_{\mathrm{LSR}}| > 210$ km s^{-1} criterion (Section 2.3). The position of the Sun is marked with a red circle. Middle column: (J_z, J_ϕ). Right column: (J_z, J_R). The larger known substructures in the Galactic halo (Section 5) that have been recognized in our sample are featured in the top row. Blue circles, dark green diamonds, pink triangles, and orange hexagons are stars associated to GSE, Sequoia, HStr, and Thamnos, respectively. The rest of the DTGs, including many new ones (see Table 3), are shown in the middle and bottom rows. DTGs with similar colors, but different symbols, have qualitatively similar dynamical properties (Section 6). In all of the plots, gray dots represent stars that were not found to be dynamically clustered. The symbols with lime-colored edges are RPE stars associated with the different groups according to their colors and symbols (Section 7).

Bonaca et al. 2020), and its (proposed) globular clusters form a tight age–metallicity relation (Myeong et al. 2018b, 2019; Massari et al. 2019; Kruijssen et al. 2020).

In order to identify potential members of GSE among our DTGs, we establish that these groups must display $\langle e \rangle \geqslant 0.8$ (see Figure 6). This criterion is similar to that of Naidu et al. (2020) and Bonaca et al. (2020). These authors have shown that stars in this range of e compose a well-behaved, strongly peaked metallicity distribution. The requirement that $e \geqslant 0.8$ had already been suggested by Myeong et al. (2018b), who considered the

distribution of globular clusters and halo stars in action space, and Mackereth et al. (2019), who analyzed the α-element abundance ratios of such high-eccentricity stars. In total, 13 of our DTGs (comprising 173 stars; Table 2) can be attributed to GSE (blue circles in the top row of Figure 5). Application of this selection yields a mean radial action $\langle J_R \rangle \gtrsim 450$ kpc km s^{-1} for each associated group. Additionally, our selected groups are contained within $-600 \lesssim \langle J_\phi \rangle$ (kpc km s^{-1}) $< +500$ (similar to Feuillet et al. 2020). The dynamical nature of GSE can be visualized in the projected action-space diagram shown in Figure 6 (top panel).
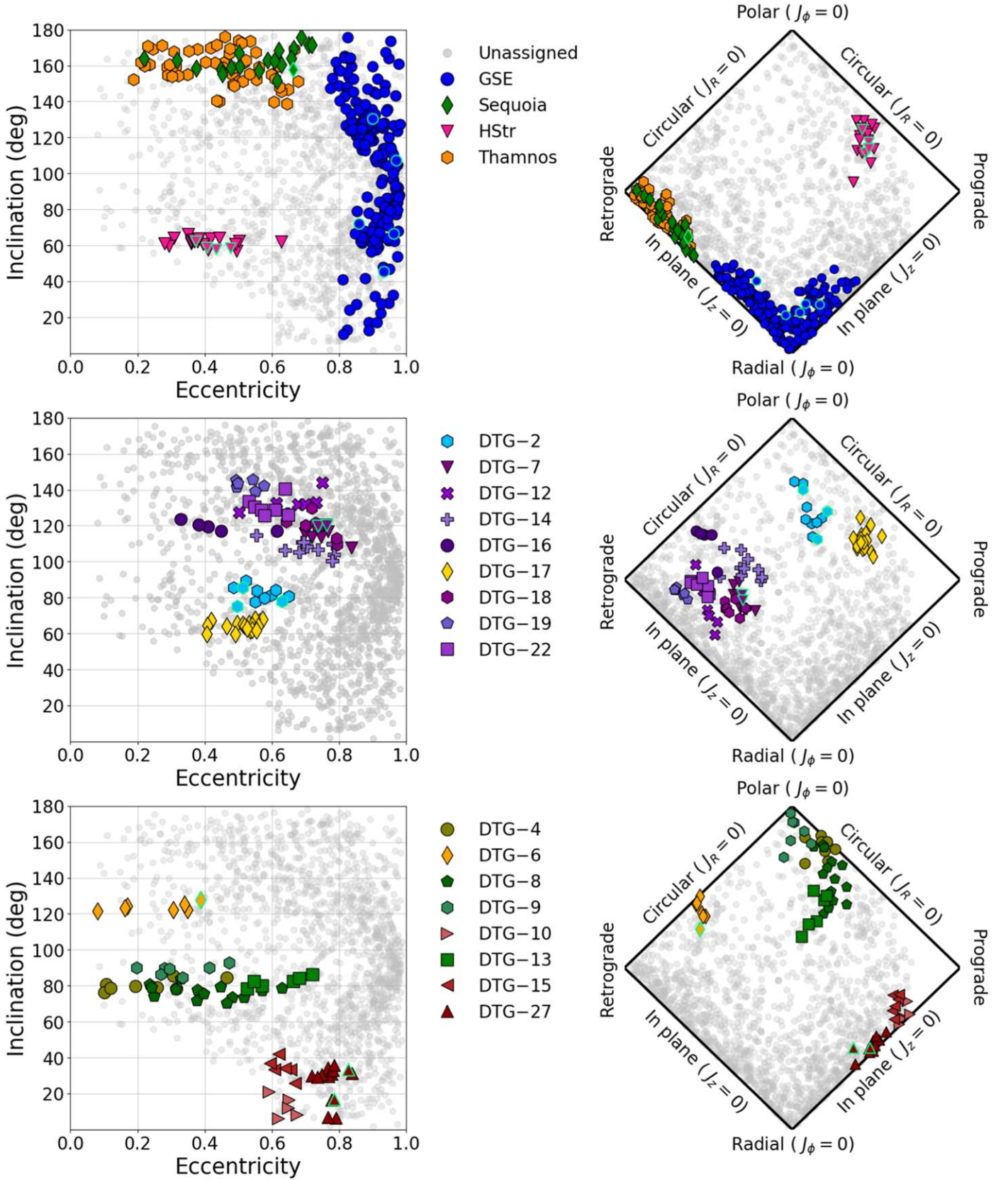
Figure 6. Left column: inclination vs. eccentricity of the VMP HK/HES sample. Stars within $0° < i < 90°$ are in prograde ($J_\phi > 0$) motion, and those in the region of $90° < i < 180°$ are retrograde ($J_\phi < 0$). Right column: projected action-space diagrams of the sample. The horizontal axis is J_ϕ/J_{total}, where $J_{total} = J_R + |J_\phi| + J_z$. The vertical axis is $(J_z - J_R)/J_{total}$. One can notice the absence of stars toward the prograde corner of the plots, due to the exclusion of objects from the disk system ($|V - V_{LSR}| > 210$ km s^{-1}; Section 2.3). The DTGs found in the VMP sample are highlighted as the colored symbols (as in Figure 5). Symbols with lime-colored edges are RPE stars associated with the different groups according to their colors and symbols (Section 7). Gray dots represent unassigned stars.

Table 2
Larger Substructures in the VMP HK/HES Sample

Substructure	Associated DTGs	Members	$\langle E \rangle$ σ_E (km^2 s^{-2})	$(\langle J_R \rangle, \langle J_\phi \rangle, \langle J_z \rangle)$ $(\sigma_{J_R}, \sigma_{J_\phi}, \sigma_{J_z})$ (kpc km s^{-1})	$\langle e \rangle$ σ_e	$\langle i \rangle$ σ_i (deg)	$(\langle v_R \rangle, \langle v_\phi \rangle, \langle v_z \rangle)$ $(\sigma_{v_R}, \sigma_{v_\phi}, \sigma_{v_z})$ (km s^{-1})	Median [Fe/H] MAD$_{[Fe/H]}$ (dex)
GSE	11,20,21,23,24,28,29, 30,34,35,36,37,38	173	-1.7×10^5 1.4×10^4	$(826, -108, 57)$ $(318, 229, 39)$	0.90 0.05	103 39	$(-7, -14, 2)$ $(162, 28, 49)$	-2.2 0.3
Sequoia	1,5	19	-1.2×10^5 1.5×10^4	$(916, -2496, 111)$ $(576, 389, 73)$	0.54 0.14	163 6	$0, -301, -39$ $(150, 44, 83)$	-2.2 0.4
HStr	3	18	-1.3×10^5 3.3×10^3	$(321, 1153, 1210)$ $(132, 134, 183)$	0.40 0.08	62 3	$(-46, 144, -198)$ $(98, 16, 167)$	-2.3 0.5
Thamnos	25,26,31,32,33	53	-1.7×10^5 5.7×10^3	$(200, -1066, 59)$ $(99, 276, 41)$	0.44 0.14	159 10	$(-4, -136, 6)$ $(70, 36, 55)$	-2.2 0.3

The GSE substructure, as we have defined it, presents stars with orbital inclinations ($i = \cos^{-1}(L_z/L)$, where L_z is the vertical component of the total angular momentum, L) spanning all possible values. In the i versus e space, it shows a "boomerang-like" shape in the top panel of Figure 6, concentrated toward high values of e. This substructure presents characteristic v_ϕ and v_R that overlap with those from the SD (Bonaca et al. 2017; Di Matteo et al. 2019; Belokurov et al. 2020; An & Beers 2020; Amarante et al. 2020a, 2020b). However, the average metallicity of the SD is $\langle [Fe/H] \rangle \approx -0.5$. Since our stars are all VMP, we expect minimal contamination from this source.

The velocity space of GSE is shown in Figure 7. As previously mentioned, this substructure presents an almost null net rotation with small dispersion ($\langle v_\phi \rangle \approx -14$ km s^{-1}; $\sigma_{v_\phi} = 28$ km s^{-1}). An interesting feature is that our velocity distribution in the radial direction is continuous, occupying $-300 < \langle v_R \rangle$ (km s^{-1}) $< +300$. This is very similar to the aforementioned characteristically huge spread in v_R presented by Belokurov et al. (2018) and others since (e.g., Koppelman et al. 2018 and Feuillet et al. 2020). The importance of GSE to the halo is further examined in Section 7.

5.2. Sequoia

Speculation that a substantial, strongly retrograde merger event could have contributed stars to the Galactic halo began to appear many years ago (Norris & Ryan 1989; Carollo et al. 2007, 2010; Beers et al. 2012). Further evidence came with the discovery of the massive globular cluster FSR 1758 (Cantat-Gaudin et al. 2018; Barbá et al. 2019). Myeong et al. (2018c) revealed an excess of stars with highly energetic, very retrograde orbits in the Galactic halo with metallicities of $-1.9 < [Fe/H] < -1.3$. Building on that, Myeong et al. (2018d) discovered a profusion of small dynamical groups of stars in this region of the (E, J_ϕ) space (and called them Rg1-4 and Rg6).

Based on the above, Myeong et al. (2019) argued that this population of stars originated from a merger event they referred to as Sequoia. These authors also claimed that a dynamically cohesive group of globular clusters (including FSR 1758) were associated to Rg1-4 and Rg6. So far, other independent analyses recognized additional Sequoia debris (Koppelman et al. 2019a; Massari et al. 2019; Matsuno et al. 2019; Dietz et al. 2020; Yuan et al. 2020b, 2020a; Monty et al. 2020; Naidu et al. 2020).

Among our dynamical groups, DTG-1 and DTG-5 (comprising a total of 19 stars, with a high confidence level, $\sim 75\%$) can be readily identified as part of the Sequoia remnant. These DTGs have $\langle E \rangle = -1.2 \times 10^5$ km^2 s^2 and $\langle J_\phi \rangle \approx -2500$ kpc km s^{-1}, so they are well within the interval established by Myeong et al. (2019). DTG-1 and DTG-5 also spread through many different values of J_R (in line with Myeong et al. 2018d), and exhibit low average vertical action: $\langle J_z \rangle \approx 145$ kpc km s^{-1}. We revisit the Sequoia event, and its possible connection to RPE stars, in Section 7.

5.3. Helmi Stream

The Helmi Stream (HStr) was one of the first dynamical groups to be found. Helmi et al. (1999) analyzed astrometric data of a small sample of metal-poor ([Fe/H] < -1.6) stars from the Hipparcos Catalog (Perryman et al. 1997), and found that some of these were significantly clumped in angular-momentum space. Further members were added by Chiba & Beers (2000) and other works since (e.g., Koppelman et al. 2018; Myeong et al. 2018a). One distinguishing aspect of this stream is that the majority of its members exhibit negative v_z, although some have positive v_z. This feature has been interpreted as the partially phase-mixed fragments of a (now) shredded satellite (Helmi 2008). The discovery of such a group, with apparently disconnected blobs in velocity space, is a demonstration of the power of searches in the integrals-of-motion space. More recent studies have focused on the chemical aspects of this substructure (Roederer et al. 2010; Aguado et al. 2020), confirming its ancient nature from its low typical metallicity ($-3.0 \lesssim [Fe/H] \lesssim -1.5$), its profile in [$\alpha$/Fe] (with a "knee" at [Fe/H] ≈ -2.0), and predominance of the r-process contribution to the enrichment of neutron-capture elements ([Sr/Ba] $\lesssim 0.0$) in the low-metallicity regime. However, the complicated story of the HStr and its progenitor is still under scrutiny (and debate; see, e.g., Koppelman et al. 2019b), and its characterization is far from being complete.

Inspection of the first row of Figure 5 allows for the immediate association of one of our larger (18 stars) and high-confidence (88%) dynamical groups (DTG-3) with the HStr. This connection is in agreement with the selection criteria delineated by Koppelman et al. (2019b). Independent efforts converge on an azimuthal velocity of $\langle v_\phi \rangle \approx 150$ km s^{-1} for this stream (Beers et al. 2017; Gaia Collaboration et al. 2018c; Koppelman et al. 2018; Myeong et al. 2018a), which is compatible with our findings ($\langle v_\phi \rangle = 144$ km s^{-1}; $\sigma_{v_\phi} = 16$ km s^{-1}). Crucially, our DTG-3 has members that are detached
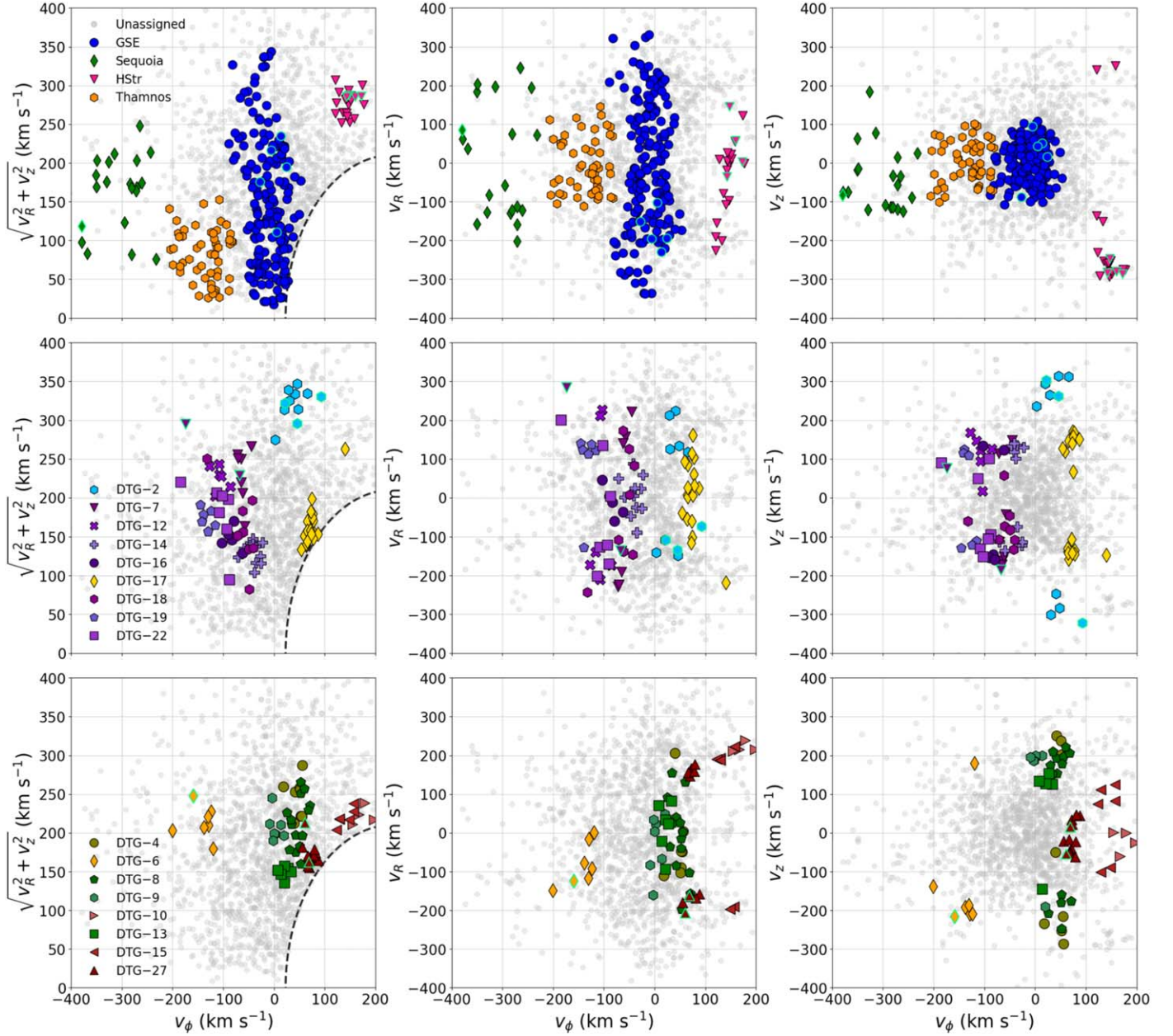
Figure 7. Velocity-space diagrams of the VMP HK/HES sample. Left panels: ($\sqrt{v_R^2 + v_z^2}$, v_ϕ). The dashed curve marks the selection boundary corresponding to the requirement that $|V - V_{\mathrm{LSR}}| > 210$ km s^{-1} (Section 2.3). Middle panels: (v_R, v_ϕ). Right panels: (v_z, v_ϕ). Upper row: GSE (blue circles; Section 5.1), Sequoia (dark green diamonds; Section 5.2), the HStr (pink triangles; Section 5.3), and Thamnos (orange hexagons; Section 5.4, Table 3). Middle and bottom rows: the rest of the DTGs, including many new ones (Section 6). The symbols with lime-colored edges are RPE stars associated with the different substructures according to their colors and symbols (Section 7). Gray dots represent unassigned stars.

in the vertical component of velocity (upper right panel of Figure 7), with the great majority presenting $v_z < 0$, which is expected for the canonical HStr. The potential enrichment of the HStr members in neutron-capture elements via the *r*-process is further explored in Section 7.

5.4. Thamnos

Koppelman et al. (2019a) suggested that another substantial, very retrograde substructure exists in the Galactic halo, which they named Thamnos. It resides in the same corner region in the projected action-space map as Sequoia (Figure 6, top panel). However, there is a marked difference in orbital energy

between Thamnos and Sequoia (upper left pane of Figure 5). The Thamnos event can be described, then, as a low-energy counterpart of Sequoia. These authors further suggested that this substructure could possibly be divided into two pieces, Thamnos 1 (Th. 1), highly retrograde and with lower metallicity, and Thamnos 2 (Th. 2), moderately retrograde and more metal-rich.

From our analysis, a total of five dynamical groups could be associated with this substructure, two of them with Th. 1 (DTG-25 and DTG-26) and the other three with Th. 2 (DTG-31, DTG-32, and DTG-33). Since Th. 1 and Th. 2 have been proposed to share the same progenitor, we present them as a single cohesive substructure (orange hexagons; top row of Figure 5). Thamnos

Table 3
New DTGs in the VMP HK/HES Sample and Their Likely Associations

DTG	Association	Members	$\langle E \rangle$ σ_E (km^2 s^{-2})	$(\langle J_R \rangle, \langle J_\phi \rangle, \langle J_z \rangle)$ $(\sigma_{J_R}, \sigma_{J_\phi}, \sigma_{J_z})$ (kpc km s^{-1})	$\langle e \rangle$ σ_e	$\langle i \rangle$ σ_i (deg)	$(\langle v_R \rangle, \langle v_\phi \rangle, \langle v_z \rangle)$ $(\sigma_{v_R}, \sigma_{v_\phi}, \sigma_{v_z})$ (km s^{-1})	Median [Fe/H] MAD$_{[Fe/H]}$ (dex)
2	New[a]	8	-1.3×10^5 5.7×10^3	(690, 293, 1878) (277, 189, 102)	0.57 0.05	83 4	(52, 35, 74) (158, 19, 292)	-2.4 0.4
4	New	8	-1.5×10^5 2.8×10^3	(85, 330, 1535) (89, 122, 110)	0.23 0.13	80 3	(-19, 46, -44) (104, 13, 237)	-2.5 0.4
8	ZY20:DTG-35	14	-1.6×10^5 3.7×10^3	(173, 361, 1039) (110, 106, 99)	0.40 0.12	77 4	(-11, 48, 51) (102, 14, 192)	-2.5 0.4
9	New	7	-1.6×10^5 2.7×10^3	(93, 25, 1299) (63, 80, 66)	0.32 0.09	89 3	(-28, 3, 139) (77, 10, 145)	-2.2 0.2
13	ZY20:DTG-39	6	-1.7×10^5 1.7×10^3	(299, 159, 709) (82, 68, 70)	0.62 0.08	82 3	(16, 20, 88) (65, 9, 114)	-2.3 0.5
6	Rg5	6	-1.5×10^5 2.7×10^3	(82, -1046, 787) (67, 60, 41)	0.23 0.11	123 2	(-75, -140, -126) (58, 30, 152)	-2.7 0.3
7	New	7	-1.5×10^5 4.2×10^3	(644, -500, 471) (118, 54, 45)	0.75 0.04	115 4	(-37, -62, -54) (200, 9, 134)	-2.5 0.4
12	New	6	-1.5×10^5 3.7×10^3	(576, -868, 285) (191, 62, 84)	0.66 0.09	134 6	(-43, -108, 112) (204, 14, 53)	-2.3 0.4
14	New	11	-1.7×10^5 1.4×10^3	(370, -326, 431) (78, 101, 61)	0.70 0.07	109 7	(6, -41, 18) (51, 14, 126)	-2.4 0.4
16	ZY20:DTG-33	5	-1.6×10^5 1.8×10^3	(161, -683, 482) (84, 94, 73)	0.44 0.11	120 3	(-12, -83, -40) (41, 15, 154)	-2.4 0.3
18	ZY20:DTG-33	8	-1.7×10^5 2.1×10^3	(473, -450, 278) (60, 82, 35)	0.73 0.05	119 6	(-31, -64, -69) (149, 30, 58)	-2.2 0.2
19	New	6	-1.6×10^5 1.9×10^3	(339, -1108, 209) (52, 58, 14)	0.53 0.04	143 2	(85, -133, -2) (104, 11, 130)	-2.4 0.6
22	ZY20:DTG-33	7	-1.7×10^5 1.2×10^3	(353, -780, 297) (62, 65, 28)	0.59 0.04	131 5	(-40, -111, -34) (156, 34, 110)	-2.2 0.4
10	New	5	-1.4×10^5 1.5×10^3	(701, 1496, 46) (86, 80, 43)	0.64 0.03	13 6	(134, 182, -19) (192, 20, 26)	-2.1 0.2
15	New	6	-1.5×10^5 3.5×10^3	(555, 1110, 146) (92, 55, 43)	0.63 0.03	34 5	(68, 140, 34) (203, 15, 102)	-2.2 0.2
27	ZY20:DTG-19	13	-1.7×10^5 8.3×10^2	(617, 590, 25) (47, 62, 12)	0.77 0.03	26 10	(-16, 73, -17) (171, 8, 40)	-2.2 0.2
17	New	18	-1.7×10^5 2.7×10^3	(223, 577, 545) (47, 63, 58)	0.51 0.05	64 2	(7, 4, 0) (94, 18, 145)	-2.3 0.4

Note. The DTGs are ordered by their numbers, but are kept grouped according to their qualitatively similar dynamical properties, as in Section 6.
[a] Tentative association with other reported substructure (Section 6.1).

can be differentiated from GSE as having predominantly retrograde motion ($\langle i \rangle \approx 160°$; $\langle J_\phi \rangle \approx -1000$ kpc km s^{-1}) and lower eccentricity ($\langle e \rangle = 0.44$; $\langle J_R \rangle \approx 200$ kpc km s^{-1}). These values are in agreement with the limits independently proposed by Naidu et al. (2020).

We note that the proliferation of small dynamical groups of stars in the low-energy, highly retrograde corner of the (E, J_ϕ) space has also been pointed out by Yuan et al. (2020b) in their own inspection of a VMP sample (their ZY20:DTG-21/24/29; see their Figure 6). Their DTGs are also comparable to ours in J_R and J_z. It is possible that many (if not all) of the groups reported by both works are pieces of the same larger substructure. This hypothesis is attractive, since it has been shown that Thamnos has a metallicity distribution that preferentially occupies the VMP regime (Koppelman et al. 2019a; Helmi 2020; Naidu et al. 2020). Thus, it would be natural to find it from examination of VMP stellar samples.

Our findings corroborate the claims that Sequoia and Thamnos are well separated in their binding energies, as can

be seen from the upper left panel of Figure 5. If one were to assume that they originated from the same merger event, it would imply that the progenitor was at least as massive as that of GSE, in conflict with their lower metallicities. For the purpose of confirming the nature of these substructures, one requires not only reliable metallicities, but other chemical abundances, especially of the α-elements, in order to explore their chemical-evolution and star formation histories. It is clear from the ongoing discussions about Sequoia/Thamnos in the literature just how difficult it is to disentangle the formation history of the Galactic halo in terms of its clumps, streams, over-densities, and their respective progenitors.

6. New Dynamical Groups

6.1. New Polar Groups

Besides the HStr (DTG-3), other dynamical groups stand out from the rest as having predominantly polar orbits (Table 3). One of these is DTG-2 (sky-blue hexagons; second row of

Figure 5). This DTG has been segregated from the rest of the polar groups as it exhibits $\langle J_R \rangle > \langle J_\phi \rangle$; it has eight members and a high confidence level (87%). One of the distinctive features of DTG-2 can be appreciated from its distribution in velocity space (Figure 7). Much like the HStr, we notice that this group is split into two blobs of v_z, one positive and one negative. We note that this DTG exhibits the highest absolute value of vertical velocity ($|v_z| \approx 300$ km s^{-1}) out of our groups. This DTG might also be a fragmented piece of the low-mass stellar-debris stream LMS-1 (Wukong), recently discovered by Yuan et al. (2020a). These authors also argued that this substructure would be reasonably metal-poor ([Fe/H] $\lesssim -1.5$), in keeping with our VMP selection. Further discussion on the nature of DTG-2 is presented in Section 7.

The remaining polar groups are DTG-4/8/9/13 (green symbols; bottom row of Figure 5). They are also mildly prograde ($v_\phi \approx +50$ km s^{-1}; Figure 7), and present characteristically low radial actions ($\langle J_R \rangle \leqslant 300$ kpc km s^{-1}; Figure 6). Out of these, DTG-8 and DTG-13 could be readily associated with ZY20: DTG-35 and ZY20:DTG-39 from Yuan et al. (2020b), respectively. These authors also identified many prograde polar groups. Future studies might reveal if this excess of polar VMP clumps could be the debris of a larger substructure or a superposition of individual small accreted systems.

6.2. New Prograde Groups

Some of our DTGs have been classified as being predominantly prograde (Table 3). Three of these are DTG-10/15/27 (red triangles; bottom row of Figure 5). The orbits of their member stars lie close to the Galactic plane ($\langle J_z \rangle \lesssim$ 150 kpc km s^{-1}; Figure 6), and exhibit moderate average eccentricities ($\langle e \rangle \geqslant 0.6$; Figure 6). All of these groups are also distinguishable from their kinematics; they present negative and positive blobs in v_R (Figure 7). However, DTG-10 and DTG-15 are rotating much faster around the Galactic center ($\langle v_\phi \rangle \gtrsim +140$ km s^{-1}; $\langle J_\phi \rangle \gtrsim +1100$ kpc km s^{-1}) than DTG-27 ($\langle v_\phi \rangle \approx +70$ km s^{-1}; $\langle J_\phi \rangle \approx +600$ kpc km s^{-1}). The rotational motions of DTG-10/15 are compatible with the value suggested for the MWTD (Carollo et al. 2019; An & Beers 2020). Comparison with both Carollo et al. (2014) and Beers et al. (2014) also points to similarities in (E, J_ϕ), but the Galactic gravitational-potential model used by these authors is different from ours, so this should be taken with caution. In addition, our kinematic cut (Section 2.3) should yield minimal contamination from stellar populations with disk-like orbits.

The more modest rotation of DTG-27 makes it overlap with both the SD and ZY20:DTG-19 (Yuan et al. 2020b) in v_ϕ and v_R. In Section 5.1, we argued that stars from the SD should represent only a minor contamination in our VMP sample, since its metallicity is $\langle$[Fe/H]$\rangle \approx -0.5$. Indeed, these objects should not affect our definition of a large substructure such as GSE, but they could produce a small clump like DTG-27. The recent demonstration that a meaningful population of extremely and ultra-metal-poor stars ([Fe/H] $\leqslant -3.0$ and $\leqslant -4.0$, respectively) permeates the Galactic thin and thick disks (Sestito et al. 2019, 2020; Di Matteo et al. 2020) underscores the possibility that these VMP stars could have acquired halo kinematics from dynamical heating mechanisms. The nature of DTG-27 is further discussed in Section 7.

The final prograde DTG out of our dynamical groups is DTG-17. Its stars are represented as yellow diamonds in the second row of Figure 5. This is a new group with 18 members (67% confidence). Considering kinematics, this DTG is similar to the green polar groups (DTG-4/8/9/13; Section 6.1). However, since its $\langle J_\phi \rangle > \langle J_z \rangle$, we present it as a predominantly prograde one. We note that Yuan et al. (2020b) also found some DTGs in this region of the energy-action space (see their Figure 6). Detailed chemical abundances from future spectroscopic efforts might hint at the origin of this excess of prograde VMP dynamical groups.

6.3. New Retrograde Groups

The majority of our new DTGs have retrograde orbits, many of which can be attributed to either Sequoia (Section 5.2) or Thamnos (Section 5.4). However, a total of eight dynamical groups are apparently unrelated to any of these better-known substructures (Table 3). The first of these is DTG-6 (orange diamonds; bottom row of Figure 5). Its stars are very retrograde ($\langle J_\phi \rangle \approx -1000$ kpc km s^{-1}), but exhibit moderate energy ($\langle E \rangle \approx -1.5 \times 10^5$ km^2 s^2). This DTG occupies the same region as the Rg5 substructure proposed by Myeong et al. (2018d), and is likely associated with it. A more in-depth examination of DTG-6/Rg5 is presented in Section 7.

The remaining retrograde DTGs are presented as purple symbols in the middle row of Figure 5. These are DTG-7/12/14/16/18/19/22. We note that this large set of DTGs occupies an intermediate region of the (E, J_ϕ) space, between GSE and Thamnos. Therefore, it is difficult to disentangle their origins from dynamics alone. For instance, DTG-7 and DTG-12 have mean radial actions in the range of GSE ($\langle J_R \rangle \gtrsim$ 500 kpc km s^{-1}), but their large values of vertical and retrograde motions, respectively, make them incompatible with this larger substructure. We revisit DTG-7 in Section 7. A similarly large set of VMP dynamical groups has already been reported by Yuan et al. (2020b). Among these, ZY20:DTG-33 strongly overlaps with three of our own DTGs (DTG-16, DTG-18, and DTG-22). Apparently, this region of the energy-action space is preferentially occupied by VMP stellar clumps; other searches, without [Fe/H] selection cuts, failed to recognize any cohesive substructures occupying it. Nevertheless, we are in urgent need of chemical-abundance information (e.g., α-elements) for the members of these DTGs in order to test whether or not these might be the remnants of low-mass system(s) that merged into the Galaxy.

7. Connections to RPE Stars

It has been argued, from a variety of standpoints, that DTGs of VMP stars are likely to be the debris of small systems shredded by the Galaxy in the past. Such low-mass (UFD and/ or dSph) galaxies have also been suggested to be the probable environments in which r-process nucleosynthesis has yielded moderate and highly r-process enhancements (Ji et al. 2016; Roederer et al. 2016, 2018; Hansen et al. 2017). Thus, it is useful to search for dynamical connections between RPE stars and the substructures identified in this work.

We have explored this possibility using the recent compilation of RPE stars from Gudin et al. (2020), as described in Section 2.4. A final list of 305 stars with suitable dynamical parameters and [Eu/Fe] $> +0.3$ has been compiled, similar to the selection from Roederer et al. (2018), but expanded to include the r-I regime. We have performed dynamical

Table 4
Associations of the VMP HK/HES Dynamical Groups with Recognized RPE Stars

DTG	Associations	Star	Confidence	[Fe/H]	[Eu/Fe]	[Ba/Eu]	[C/Fe]$_c$	Class
1	Sequoia	2MASS J11444086−0409511	20%	−2.52	+0.58	−0.84	+0.33	r-I
2	New[a]	2MASS J00453930−7457294	21%	−2.00	+0.55	−0.18	+0.98	r-I/CEMP-r
		2MASS J00413026−4058547	46%	−2.58	+0.38	−0.65	+0.20	r-I
		2MASS J02274104−0519230	78%	−2.38	+0.42	−0.60	+0.08	r-I
3	HStr	HD 175305	100%	−1.50	+0.44	−0.32		r-I
		HD 119516	100%	−2.26	+0.34	−0.36	+0.28	r-I
		BD+30:2611	100%	−1.40	+0.45	−0.37		r-I
		2MASS J03270229 + 0132322	66%	−2.39	+1.07	−0.57	+0.36	r-II
6	Rg5	SDSS J235718.91−005247.8	22%	−3.36	+1.92	−0.80	+0.43	r-II
7	New	BPS BS 16089−0013	39%	−2.70	+0.46	−0.59	+0.66	r-I
		2MASS J17060555 + 0412354	20%	−2.71	+0.50	−0.45	+0.60	r-I
24	GSE	BPS CS 22968−0026	91%	−2.57	+0.58	−1.09	−0.09	r-I
		2MASS J00482431−1041309	21%	−2.50	+0.45	−0.36	+0.47	r-I
28		2MASS J08393460−2122069	55%	−1.94	+0.42	−0.29	+0.14	r-I
30		2MASS J18562774−7251331	28%	−2.26	+0.32	−0.33	+0.24	r-I
		2MASS J00073817−0345509	22%	−2.09	+0.73	−0.62	+0.17	r-II
27	ZY20:DTG-19	HD 115444	100%	−2.99	+0.85	−0.67	+0.32	r-II
		2MASS J20005766−2541488	20%	−2.05	+0.40	−0.05	+0.27	r-I

Note. The DTGs are ordered by their numbers, but are kept grouped according to their dynamical properties (Section 6) and including the larger structures (Section 5).
[a] Tentative association with other reported substructure (Section 6.1). [C/Fe]$_c$ values have been corrected for their evolutionary status (Placco et al. 2014b).

calculations within the same scheme delineated in Section 3. Regarding the cluster assignments, we have carried out 1000 Monte Carlo realizations of their (E, J_R, J_ϕ, J_z), and fed these generated sets back into the cluster hierarchy tree (Section 4.1). This exercise is analogous to the one that has been applied to evaluate the statistical significance of our DTGs and estimate their confidence levels. Again, we have only considered stars with at least 20% membership probability. We have retained stars that are both RPE and CEMP (CEMP-r), since the astrophysical site(s) for the production of this abundance pattern is still under investigation (see, e.g., Frebel 2018).

A total of 18 RPE stars have been associated with our DTGs (Table 4); some are members of previously known groups and others of our newly discovered ones. The locations of these stars in comparison to their respective DTGs can be appreciated in Figures 5, 6, and 7. They are represented with the same colors and symbols of their associated groups, but with lime-colored edges.

Out of these RPE stars, five of them have been associated to dynamical groups that belong to GSE. Two of these RPE stars have also been clustered together by Gudin et al. (2020) from their dynamics. All of these stars are contained within the ranges +0.30 < [Eu/Fe] ≲ +0.70 and −2.5 < [Fe/H] < −2.0. These [Eu/Fe] ratios are comparable to RPE stars from the Ursa Minor dSph galaxy (Sadakane et al. 2004; Cohen & Huang 2010) for the same metallicity interval. However, stars from Ursa Minor present systematically lower abundance values of [Ba/Eu]. Yuan et al. (2020b) had already hinted at a connection between RPE stars and GSE from their dynamics. The accumulated evidence points to GSE (and/or its progenitor systems) as an important source of such stars to the Galaxy.

From examination of retrograde groups in our VMP sample, an r-I star is possibly connected to the Sequoia remnant (DTG-1). Additionally, our DTG-6 (compatible with Rg5;

Myeong et al. 2018d) has been shown to be potentially associated to one of the most extremely RPE stars (r-II; [Eu/Fe] = +1.92) known to date. This is in line with Yuan et al. (2020b), who had already assigned the same object to the Rg5 debris. The level of r-process enrichment of this star is comparable to the RPE UFD galaxy Reticulum II (Ji et al. 2016). Likewise, DTG-7 appears to be associated with two RPE (both r-I) stars. The similarities in [Fe/H], [Eu/Fe], and [Ba/Eu] for these objects can be seen in Table 4. Interestingly, these abundance ratios are also comparable to those of RPE stars associated with the GSE substructure.

Only one of our predominantly prograde groups, DTG-27, has been associated with two RPE stars, one r-I and the other r-II. This finding is in agreement with Gudin et al. (2020), who independently attributed both of these stars to the same dynamical group. In Section 6.2, we pointed out that a group of VMP stars with very similar orbital properties to DTG-27 had already been found (ZY20:DTG-19; Yuan et al. 2020b). Member stars of this DTG should be primary targets for future studies, as they could provide clues on the early nucleosynthesis processes that operated in this component of the Galactic halo system.

Among our polar groups, three RPE stars, all r-I (one being of the CEMP-r subclass), have been attributed to DTG-2. This is even more interesting, considering the tentative connection between this dynamical group and the Yuan et al. (2020a) low-mass stellar-debris stream LMS-1 (see also Naidu et al. 2020; Section 6.1). Future chemical-abundance analysis would be useful to confirm this linkage.

One of the most intriguing of our findings is that four RPE stars have been associated with the HStr (DTG-3). Three of these stars have very similar [Eu/Fe] ratios ([Eu/Fe] ≈ +0.40; r-I), and the other is more enriched in r-process elements ([Eu/Fe] = +1.07; r-II). The excess of RPE stars in this

substructure is also consistent with recent spectroscopic efforts (Roederer et al. 2010; Aguado et al. 2020). In both works, the authors argued that the enrichment in neutron-capture elements of the member stars of the HStr was dominated by the *r*-process, based on their [Sr/Ba] patterns at the VMP end. Clearly, more detailed elemental-abundance studies of stars from the HStr would be useful to better constrain the chemical-evolution history of its progenitor.

8. Conclusions

In this work, we have considered the dynamical properties of the VMP ([Fe/H] $\lesssim -2.0$) stars primarily selected from the HK/HES surveys. We have employed a sample of 1526 VMP stars from the Galactic halo with suitably accurate dynamical parameters to perform a substructure search in the energy-action space. This metallicity cut allows us to find groups of stars that have conceivably been born in UFD and dSph galaxies that merged with the MW in the past.

Our analysis has been carried out with the algorithm HDBSCAN, where the clustering has been performed in the parameter space of (E, J_R, J_ϕ, J_z). We have identified 38 significant DTGs, comprising ~400 stars. We have been able to recover larger, previously known substructures such as GSE (Belokurov et al. 2018; Helmi et al. 2018), Sequoia (Myeong et al. 2019), the HStr (Helmi et al. 1999), and Thamnos (Koppelman et al. 2019a), as well as smaller groups from Myeong et al. (2018d) and Yuan et al. (2020b), and a number of newly identified ones. We have also investigated possible connections between our DTGs and RPE stars compiled by Gudin et al. (2020). In total, 18 such stars have been associated to our groups, including several of the new ones. The main results from our analysis are summarized below.

1. All of the aforementioned larger structures present meaningful numbers of VMP stars (at least ~20 each) within the HK/HES sample. Future high-precision abundance analyses of these objects might allow us to constrain the conditions of the star-forming environments and chemical evolution of their progenitors.

2. The GSE substructure is associated with 173 of our stars in 13 DTGs. We have also provided evidence that five *r*-I/*r*-II stars could be associated with it. This is in agreement with Gudin et al. (2020); these authors also dynamically clustered together two of these stars, in an independent analysis. These results indicate that the GSE progenitor might have been an important source of RPE stars to the Galactic halo.

3. The distribution of our DTGs in the energy-action space favors the hypothesis that Sequoia and Thamnos are indeed distinct entities, being widely separated in energy, in line with other recent results (Koppelman et al. 2019a; Naidu et al. 2020; Monty et al. 2020). Also, DTG-1 (Sequoia) has been associated with one *r*-I star.

4. The HStr has been recovered, in agreement with the literature (Koppelman et al. 2018, 2019b; Myeong et al. 2018a). It has also been associated with four RPE stars. This could be another strong indication that, in the very low-metallicity regime, the progenitor of the HStr experienced enrichment in neutron-capture elements predominantly via the *r*-process, in accord with other

recent results from chemical-abundance analyses (Roederer et al. 2010; Aguado et al. 2020).

5. Some of our DTGs have highly polar orbits. One of these (DTG-2) has been tentatively associated with the low-mass stellar stream LMS-1 (or Wukong; see Naidu et al. 2020) recently discovered by Yuan et al. (2020a). Surprisingly, three RPE stars have been attributed to this DTG. The rest of our polar DTGs are mildly prograde, and some are compatible with dynamical groups from Yuan et al. (2020b).

6. Four of our DTGs have been classified as predominantly prograde. One of them, DTG-27, is associated with two RPE stars, in agreement with Gudin et al. (2020). Yuan et al. (2020b) identified a dynamical group with similar dynamical properties (YZ20:DTG-19). Its location in the energy-action and velocity spaces suggest that this DTG could be related to the dynamically heated disk of the Galaxy.

7. Many of our smaller groups are strongly retrograde and have moderate energies. One of them (DTG-6) is comparable to Rg5 (Myeong et al. 2018d) in both the energy-action and velocity spaces. One of the most extremely RPE stars known has been associated to this DTG; Yuan et al. (2020b) also argued that this *r*-II star is potentially associated with Rg5. Seven other DTGs present predominantly retrograde orbits. Among these, DTG-7 has been associated with two *r*-I stars with very similar [Eu/Fe] and [Ba/Eu] ratios; its member stars are clearly compelling targets for future studies.

The complex formation history of the Galactic stellar halo has been a long-standing mystery. However, large astrometric, photometric, and spectroscopic surveys have now provided the tools for Galactic archaeologists to start solving this puzzle. Ancient very metal-poor stars play a crucial role in reconstructing the formation history of the Milky Way's halo, and provide clues about the environments in which the early nucleosynthesis of heavy elements took place. The VMP field stars in the HK/HES (and other surveys) have the enormous advantage that they are much closer (and hence significantly brighter) than any surviving satellite galaxy. Thus, the methodology described in this work can be applied to future (and much larger) stellar samples with more complete chemical-abundance information, helping to unveil and refine our understanding of the assembly history of the Milky Way.

Appendix
Initial and Final Samples of VMP Stars from the HK/HES Surveys

A.1. Initial Sample

Table 5 provides the relevant information for the initial sample (Section 2), as well as their derived atmospheric parameters, including metallicity (in the form of [Fe/H]) and carbonicity ([C/Fe]). We note that a small fraction (∼3%) of these stars are quite cool and carbon enhanced, with $T_{\rm eff} \leqslant 4500$ K and [C/Fe] (and/or $[C/Fe]_c$) $\geqslant +0.7$. Caution is urged when considering the listed values of [Fe/H], [C/Fe], and $[C/Fe]_c$ for these stars, due to the presence of "carbon-veiling" in cooler CEMP stars, which depresses the continuum in the region of the Ca II K line that has a dominant influence on the metallicity estimation (see discussion in Yoon et al. 2020). These effects can be mitigated by application of procedures similar to those described in Yoon et al., which are currently being refined, and will be employed for the present data in the near future.

The first column of the table lists the 2MASS (Skrutskie et al. 2006) names, when available. The second and third columns list the HK and HES names. Other names for stars that do not appear in 2MASS or the HK and/or HES surveys are provided in the fourth column. The *V*-band magnitude is listed as well, based on information reported in the literature, supplemented, where needed, with transformed values from Gaia DR2 photometry (Evans et al. 2018), or estimated from the HES prism plates.

A.2. Final Sample

Table 6 provides the stars contained in the final sample (Section 2). The measured RVs (corrected to the heliocentric frame) from the medium-resolution spectroscopy are listed, along with the Gaia DR2 values, where available. The StarHorse distance estimates and their relative errors are from Anders et al. (2019), as described in Section 2.3. Proper motions are taken from Gaia Collaboration et al. (2018a). The primary derived dynamical properties used in our analysis (Section 3) are also listed.

Table 5
Initial Sample of the VMP HK/HES Stars

Name (2MASS)	Name (HK)	Name (HES)	Name (other)	R.A. (deg)	Decl. (deg)	*V* mag	$T_{\rm eff}$ (K)	log *g* (cgs)	[Fe/H]	[C/Fe]	$[C/Fe]_c$
00000093−3037362	⋯	HE 2357−3054	⋯	0.0039	−30.6267	16.3	4358	0.75	−3.50[a]	+3.38[a]	+3.42[a]
00001345−2705322	⋯	HE 2357−2722	⋯	0.0560	−27.0923	16.8	6128	3.30	−1.90	−0.08	−0.08
00003365−4158196	⋯	HE 2357−4215	⋯	0.1402	−41.9721	16.6	6630	3.73	−2.48	+1.11	+1.11
00003955−1622127	CS 29517−0037	⋯	⋯	0.1649	−16.3702	14.7	6168	3.49	−2.21	+1.16	+1.16
00004942−2914458	CS 22961−0019	⋯	⋯	0.2060	−29.2461	14.1	5752	4.18	−1.88	+0.89	+0.89
00024896−1834447	CS 30304−0033	⋯	⋯	0.2800	−18.5790	13.6	6544	3.67	−2.44	<+1.11	<+1.11
00011421−2230539	⋯	HE 2358−2247	⋯	0.3092	−22.5150	16.1	6251	3.65	−2.07	+1.06	+1.06
00012661−0036118	⋯	HE 2358−0052	⋯	0.3609	−0.6033	16.4	6330	3.43	−1.81	+1.04	+1.04
00014549−0549465	CS 22957−0022	⋯	⋯	0.4395	−5.8296	13.3	5467	3.02	−2.85	+0.79	+0.79
00014710−1347251	CS 31060−0062	⋯	⋯	0.4463	−13.7903	14.0	6257	3.36	−1.84	<−0.06	<−0.06

Note. $[C/Fe]_c$ values have been corrected for their evolutionary status (Placco et al. 2014b).
[a] CEMP stars with $T_{\rm eff} \leqslant 4500$ K. Their [Fe/H], [C/Fe], and $[C/Fe]_c$ ratios should be taken with caution (Section A.1).

(This table is available in its entirety in machine-readable form.)
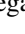
Table 6
Final Sample of the VMP HK/HES Stars

Name	RV	RV$_{\rm Gaia}$	D (err)	PM$_{\rm R.A.}$	PM$_{\rm Decl.}$	E ×10^5	(J$_R$, J$_\phi$, J$_z$) ×10^3	e	i	(v$_R$, v$_\phi$, v$_z$)
(2MASS)	(km s^{-1})	(km s^{-1})	(kpc)	(mas yr^{-1})	(mas yr^{-1})	(km^2 s^{-2})	(kpc km s^{-1})		(deg)	(km s^{-1})
00003955−1622127	−126	⋯	1.87 (0.27)	20.15	−28.54	−1.74	(0.24, −0.85, 0.09)	0.53	154.9	(29.14, −105.03, 38.38)
00014549−0549465	−32	⋯	3.33 (0.55)	8.20	−26.45	−1.40	(0.13, −1.38, 0.87)	0.28	127.2	(−139.43, −165.20, −153.78)
00020802−0249121	−135	−122.6	0.83 (0.07)	−37.55	−91.35	−1.25	(2.07, −0.17, 0.02)	0.97	123.5	(−336.41, −21.02, 2.83)
00023699−6545212	160	⋯	6.30 (1.03)	−2.90	−6.21	−1.53	(0.55, −0.37, 0.66)	0.72	110.1	(−210.65, −58.73, 23.58)
00025685−4101045	123	⋯	1.46 (0.15)	0.77	−44.29	−1.66	(0.59, −0.47, 0.11)	0.79	130.4	(−168.76, −60.25, −38.09)
00030319−4020529	124	⋯	0.78 (0.04)	−34.77	−96.56	−1.35	(1.63, −0.31, 0.03)	0.94	136.6	(−310.42, −38.31, −7.06)
00031324−0249074	−10	⋯	1.27 (0.17)	27.98	−44.47	−1.70	(0.24, −0.49, 0.48)	0.55	113.1	(1.81, −59.24, −134.86)
00033134−0444224	−100	⋯	1.20 (0.15)	38.64	−22.27	−1.73	(0.74, −0.15, 0.03)	0.94	131.4	(123.78, −17.59, 3.10)
00041037−1539281	−176	⋯	0.68 (0.04)	88.61	46.79	−0.97	(2.77, 1.55, 0.50)	0.83	44.2	(336.68, 189.78, 152.13)
00045244−3413372	−178	⋯	1.81 (0.29)	−5.31	−18.91	−1.49	(0.27, 0.88, 0.74)	0.46	58.9	(−95.88, 112.66, 209.22)

(This table is available in its entirety in machine-readable form.)

ORCID iDs

Guilherme Limberg ⓘ https://orcid.org/0000-0002-9269-8287
Silvia Rossi ⓘ https://orcid.org/0000-0001-7479-5756
Timothy C. Beers ⓘ https://orcid.org/0000-0003-4573-6233
Hélio D. Perottoni ⓘ https://orcid.org/0000-0002-0537-4146
Angeles Pérez-Villegas ⓘ https://orcid.org/0000-0002-5974-3998
Rafael M. Santucci ⓘ https://orcid.org/0000-0002-7529-1442
Yuri Abuchaim ⓘ https://orcid.org/0000-0002-6838-2178
Vinicius M. Placco ⓘ https://orcid.org/0000-0003-4479-1265
Young Sun Lee ⓘ https://orcid.org/0000-0001-5297-4518
Norbert Christlieb ⓘ https://orcid.org/0000-0002-4043-2727
John E. Norris ⓘ https://orcid.org/0000-0002-7900-5554
Michael S. Bessell ⓘ https://orcid.org/0000-0001-7801-1410
Sean G. Ryan ⓘ https://orcid.org/0000-0001-9069-5122
Ronald Wilhelm ⓘ https://orcid.org/0000-0002-4792-7722
Jaehyon Rhee ⓘ https://orcid.org/0000-0001-9214-7437
Anna Frebel ⓘ https://orcid.org/0000-0002-2139-7145

References

Abohalima, A., & Frebel, A. 2018, ApJS, 238, 36
Aguado, D. S., Myeong, G. C., Belokurov, V., et al. 2020, MNRAS, 500, 889
Amarante, J. A. S., Beraldo e Silva, L., Debattista, V. P., & Smith, M. C. 2020a, ApJL, 891, L30
Amarante, J. A. S., Smith, M. C., & Boeche, C. 2020b, MNRAS, 492, 3816
An, D., & Beers, T. C. 2020, ApJ, 897, 39
An, D., Beers, T. C., Johnson, J. A., et al. 2013, ApJ, 763, 65
An, D., Beers, T. C., Santucci, R. M., et al. 2015, ApJL, 813, L28
Anders, F., Khalatyan, A., Chiappini, C., et al. 2019, A&A, 628, A94
Aoki, W., Beers, T. C., Christlieb, N., et al. 2007, ApJ, 655, 492
Asplund, M., Grevesse, N., Sauval, A. J., & Scott, P. 2009, ARA&A, 47, 481
Astropy Collaboration, Robitaille, T. P., Tollerud, E. J., et al. 2013, A&A, 558, A33
Astropy Collaboration, Price-Whelan, A. M., Sipőcz, B. M., et al. 2018, AJ, 156, 123
Barbá, R. H., Minniti, D., Geisler, D., et al. 2019, ApJL, 870, L24
Beers, T. C., Carollo, D., Ivezić, Ž, et al. 2012, ApJ, 746, 34
Beers, T. C., Drilling, J. S., Rossi, S., et al. 2002, AJ, 124, 931
Beers, T. C., Flynn, K., & Gebhardt, K. 1990a, AJ, 100, 32
Beers, T. C., Norris, J. E., Placco, V. M., et al. 2014, ApJ, 794, 58
Beers, T. C., Placco, V. M., Carollo, D., et al. 2017, ApJ, 835, 81
Beers, T. C., Preston, G. W., & Shectman, S. A. 1985, AJ, 90, 2089
Beers, T. C., Preston, G. W., & Shectman, S. A. 1992, AJ, 103, 1987
Beers, T. C., Preston, G. W., Shectman, S. A., & Kage, J. A. 1990b, AJ, 100, 849
Beers, T. C., Rossi, S., Norris, J. E., Ryan, S. G., & Shefler, T. 1999, AJ, 117, 981
Beers, T. C., Rossi, S., O'Donoghue, D., et al. 2001, MNRAS, 320, 451
Belokurov, V., Erkal, D., Evans, N. W., Koposov, S. E., & Deason, A. J. 2018, MNRAS, 478, 611
Belokurov, V., Sanders, J. L., Fattahi, A., et al. 2020, MNRAS, 494, 3880
Bidelman, W. P., & MacConnell, D. J. 1973, AJ, 78, 687
Binney, J. 2012, MNRAS, 426, 1324
Binney, J., & Tremaine, S. 2008, Galactic Dynamics: Second Edition (Princeton, NJ: Princeton Univ. Press)
Bland-Hawthorn, J., & Gerhard, O. 2016, ARA&A, 54, 529
Bonaca, A., Conroy, C., Cargile, P. A., et al. 2020, ApJL, 897, L18
Bonaca, A., Conroy, C., Wetzel, A., Hopkins, P. F., & Kereš, D. 2017, ApJ, 845, 101
Bond, H. E. 1970, ApJS, 22, 117
Bond, H. E. 1980, ApJS, 44, 517
Campello, R. J. G. B., Moulavi, D., Zimek, A., & Sander, J. 2015, ACM Trans. Knowl. Discov. Data, 10, 51
Cantat-Gaudin, T., Jordi, C., Vallenari, A., et al. 2018, A&A, 618, A93
Carollo, D., Beers, T. C., Chiba, M., et al. 2010, ApJ, 712, 692
Carollo, D., Beers, T. C., Lee, Y. S., et al. 2007, Natur, 450, 1020
Carollo, D., Chiba, M., Ishigaki, M., et al. 2019, ApJ, 887, 22
Carollo, D., Freeman, K., Beers, T. C., et al. 2014, ApJ, 788, 180
Cayrel, R., Depagne, E., Spite, M., et al. 2004, A&A, 416, 1117
Chiba, M., & Beers, T. C. 2000, AJ, 119, 2843

Christlieb, N., Bessell, M. S., Beers, T. C., et al. 2002, Natur, 419, 904
Christlieb, N., Schörck, T., Frebel, A., et al. 2008, A&A, 484, 721
Cohen, J. G., Christlieb, N., McWilliam, A., et al. 2008, ApJ, 672, 320
Cohen, J. G., & Huang, W. 2010, ApJ, 719, 931
de Jong, J. T. A., Yanny, B., Rix, H.-W., et al. 2010, ApJ, 714, 663
Di Matteo, P., Haywood, M., Lehnert, M. D., et al. 2019, A&A, 632, A4
Di Matteo, P., Spite, M., Haywood, M., et al. 2020, A&A, 636, A115
Dietz, S. E., Yoon, J., Beers, T. C., & Placco, V. M. 2020, ApJ, 894, 34
Evans, D. W., Riello, M., De Angeli, F., et al. 2018, A&A, 616, A4
Ezzeddine, R., Rasmussen, K., Frebel, A., et al. 2020, ApJ, 898, 150
Feuillet, D. K., Feltzing, S., Sahlholdt, C. L., & Casagrande, L. 2020, MNRAS, 497, 109
Frebel, A. 2018, ARNPS, 68, 237
Frebel, A., Aoki, W., Christlieb, N., et al. 2005, Natur, 434, 871
Frebel, A., Christlieb, N., Norris, J. E., et al. 2006, ApJ, 652, 1585
Gaia Collaboration, Prusti, T., de Bruijne, J. H. J., et al. 2016a, A&A, 595, A1
Gaia Collaboration, Brown, A. G. A., Vallenari, A., et al. 2016b, A&A, 595, A2
Gaia Collaboration, Brown, A. G. A., Vallenari, A., et al. 2018a, A&A, 616, A1
Gaia Collaboration, Babusiaux, C., van Leeuwen, F., et al. 2018b, A&A, 616, A10
Gaia Collaboration, Helmi, A., van Leeuwen, F., et al. 2018c, A&A, 616, A12
Gallart, C., Bernard, E. J., Brook, C. B., et al. 2019, NatAs, 3, 932
Gravity Collaboration, Abuter, R., Amorim, A., et al. 2019, A&A, 625, L10
Gudin, D., Shank, D., Beers, T. C., et al. 2020, arXiv:2012.13808
Hansen, C. J., Hansen, T. T., Koch, A., et al. 2019, A&A, 623, A128
Hansen, T. T., Holmbeck, E. M., Beers, T. C., et al. 2018, ApJ, 858, 92
Hansen, T. T., Simon, J. D., Marshall, J. L., et al. 2017, ApJ, 838, 44
Hayes, C. R., Majewski, S. R., Shetrone, M., et al. 2018, ApJ, 852, 49
Haywood, M., Di Matteo, P., Lehnert, M. D., et al. 2018, ApJ, 863, 113
Helmi, A. 2008, A&ARv, 15, 145
Helmi, A. 2020, ARA&A, 58, 205
Helmi, A., Babusiaux, C., Koppelman, H. H., et al. 2018, Natur, 563, 85
Helmi, A., Veljanoski, J., Breddels, M. A., Tian, H., & Sales, L. V. 2017, A&A, 598, A58
Helmi, A., White, S. D. M., de Zeeuw, P. T., & Zhao, H. 1999, Natur, 402, 53
Hill, V., Plez, B., Cayrel, R., et al. 2002, A&A, 387, 560
Holmbeck, E. M., Hansen, T. T., Beers, T. C., et al. 2020, ApJS, 249, 30
Hunter, J. D. 2007, CSE, 9, 90
Ibata, R. A., Gilmore, G., & Irwin, M. J. 1994, Natur, 370, 194
Ji, A. P., Frebel, A., Chiti, A., & Simon, J. D. 2016, Natur, 531, 610
Kim, Y. K., Lee, Y. S., & Beers, T. C. 2019, ApJ, 882, 176
Koppelman, H., Helmi, A., & Veljanoski, J. 2018, ApJL, 860, L11
Koppelman, H. H., Helmi, A., Massari, D., Price-Whelan, A. M., & Starkenburg, T. K. 2019a, A&A, 631, L9
Koppelman, H. H., Helmi, A., Massari, D., Roelenga, S., & Bastian, U. 2019b, A&A, 625, A5
Kruijssen, J. M. D., Pfeffer, J. L., Chevance, M., et al. 2020, MNRAS, 498, 2472
Lee, Y. S., Beers, T. C., Allende Prieto, C., et al. 2011, AJ, 141, 90
Lee, Y. S., Beers, T. C., Kim, Y. K., et al. 2017, ApJ, 836, 91
Lee, Y. S., Beers, T. C., & Kim, Y. K. 2019, ApJ, 885, 102
Lee, Y. S., Beers, T. C., Masseron, T., et al. 2013, AJ, 146, 132
Lee, Y. S., Beers, T. C., Sivarani, T., et al. 2008a, AJ, 136, 2022
Lee, Y. S., Beers, T. C., Sivarani, T., et al. 2008b, AJ, 136, 2050
Li, H., Tan, K., & Zhao, G. 2018, ApJS, 238, 16
Lindegren, L., Hernández, J., Bombrun, A., et al. 2018, A&A, 616, A2
Mackereth, J. T., Schiavon, R. P., Pfeffer, J., et al. 2019, MNRAS, 482, 3426
Marshall, J. L., Hansen, T., Simon, J. D., et al. 2019, ApJ, 882, 177
Massari, D., Koppelman, H. H., & Helmi, A. 2019, A&A, 630, L4
Matsuno, T., Aoki, W., & Suda, T. 2019, ApJL, 874, L35
McInnes, L., Healy, J., & Astels, S. 2017, JOSS, 2, 205
McMillan, P. J. 2017, MNRAS, 465, 76
Monty, S., Venn, K. A., Lane, J. M. M., Lokhorst, D., & Yong, D. 2020, MNRAS, 497, 1236
Myeong, G. C., Evans, N. W., Belokurov, V., Amorisco, N. C., & Koposov, S. E. 2018a, MNRAS, 475, 1537
Myeong, G. C., Evans, N. W., Belokurov, V., Sanders, J. L., & Koposov, S. E. 2018b, ApJL, 863, L28
Myeong, G. C., Evans, N. W., Belokurov, V., Sanders, J. L., & Koposov, S. E. 2018c, ApJL, 856, L26
Myeong, G. C., Evans, N. W., Belokurov, V., Sanders, J. L., & Koposov, S. E. 2018d, MNRAS, 478, 5449
Myeong, G. C., Vasiliev, E., Iorio, G., Evans, N. W., & Belokurov, V. 2019, MNRAS, 488, 1235

Naidu, R. P., Conroy, C., Bonaca, A., et al. 2020, ApJ, 901, 48
Nissen, P. E., & Schuster, W. J. 2010, A&A, 511, L10
Norris, J. 1986, ApJS, 61, 667
Norris, J., Bessell, M. S., & Pickles, A. J. 1985, ApJS, 58, 463
Norris, J. E., & Ryan, S. G. 1989, ApJL, 336, L17
Norris, J. E., Ryan, S. G., & Beers, T. C. 1996, ApJS, 107, 391
Pedregosa, F., Varoquax, G., Gramfort, A., et al. 2012, arXiv:1201.0490
Perryman, M. A. C., Lindegren, L., Kovalevsky, J., et al. 1997, A&A, 500, 501
Placco, V. M., Beers, T. C., Santucci, R. M., et al. 2018, AJ, 155, 256
Placco, V. M., Frebel, A., Beers, T. C., et al. 2014a, ApJ, 781, 40
Placco, V. M., Frebel, A., Beers, T. C., & Stancliffe, R. J. 2014b, ApJ, 797, 21
Placco, V. M., Kennedy, C. R., Beers, T. C., et al. 2011, AJ, 142, 188
Placco, V. M., Kennedy, C. R., Rossi, S., et al. 2010, AJ, 139, 1051
Placco, V. M., Santucci, R. M., Beers, T. C., et al. 2019, ApJ, 870, 122
Queiroz, A. B. A., Anders, F., Chiappini, C., et al. 2020, A&A, 638, A76
Queiroz, A. B. A., Anders, F., Santiago, B. X., et al. 2018, MNRAS, 476, 2556
Rhee, J. 2001, PASP, 113, 1569
Rhee, J., Beers, T. C., & Irwin, M. J. 1999, AAS Meeting, 194, 84.11
Roederer, I. U., Hattori, K., & Valluri, M. 2018, AJ, 156, 179
Roederer, I. U., Mateo, M., Bailey, J. I., et al. 2016, AJ, 151, 82
Roederer, I. U., Preston, G. W., Thompson, I. B., et al. 2014, AJ, 147, 136
Roederer, I. U., Sneden, C., Thompson, I. B., Preston, G. W., & Shectman, S. A. 2010, ApJ, 711, 573
Rossi, S., Beers, T. C., Sneden, C., et al. 2005, AJ, 130, 2804
Ryan, S. G., & Smith, I. M. 2003, MNRAS, 341, 199
Sadakane, K., Arimoto, N., Ikuta, C., et al. 2004, PASJ, 56, 1041
Sakari, C. M., Placco, V. M., Farrell, E. M., et al. 2018, ApJ, 868, 110
Schlafly, E. F., & Finkbeiner, D. P. 2011, ApJ, 737, 103
Schlaufman, K. C., Rockosi, C. M., Allende Prieto, C., et al. 2009, ApJ, 703, 2177
Schlaufman, K. C., Rockosi, C. M., Lee, Y. S., et al. 2012, ApJ, 749, 77
Schlaufman, K. C., Rockosi, C. M., Lee, Y. S., Beers, T. C., & Allende Prieto, C. 2011, ApJ, 734, 49
Schlegel, D. J., Finkbeiner, D. P., & Davis, M. 1998, ApJ, 500, 525
Schönrich, R., Binney, J., & Dehnen, W. 2010, MNRAS, 403, 1829
Searle, L., & Zinn, R. 1978, ApJ, 225, 357
Sestito, F., Longeard, N., Martin, N. F., et al. 2019, MNRAS, 484, 2166
Sestito, F., Martin, N. F., Starkenburg, E., et al. 2020, MNRAS, 497, L7
Simon, J. D. 2019, ARA&A, 57, 375
Skrutskie, M. F., Cutri, R. M., Stiening, R., et al. 2006, AJ, 131, 1163
Somerville, R. S., & Davé, R. 2015, ARA&A, 53, 51
Sommer-Larsen, J., Beers, T. C., Flynn, C., Wilhelm, R., & Christensen, P. R. 1997, ApJ, 481, 775
Spergel, D. N., Bean, R., Dore, O., et al. 2007, ApJS, 170, 377
Trick, W. H., Coronado, J., & Rix, H.-W. 2019, MNRAS, 484, 3291
van der Walt, S., Colbert, S. C., & Varoquaux, G. 2011, CSE, 13, 22
Vasiliev, E. 2019, MNRAS, 482, 1525
Virtanen, P., Gommers, R., Oliphant, T. E., et al. 2020, Nat. Method, 17, 261
Xiang, M. S., Liu, X. W., Yuan, H. B., et al. 2015, MNRAS, 448, 822
Yanny, B., Rockosi, C., Newberg, H. J., et al. 2009, AJ, 137, 4377
Yoon, J., Whitten, D. D., Beers, T. C., et al. 2020, ApJ, 894, 7
York, D. G., Adelman, J., Anderson, J. E. J., et al. 2000, AJ, 120, 1579
Yuan, Z., Chang, J., Beers, T. C., & Huang, Y. 2020a, ApJL, 898, L37
Yuan, Z., Myeong, G. C., Beers, T. C., et al. 2020b, ApJ, 891, 39
Yuan, Z., Smith, M. C., Xue, X.-X., et al. 2019, ApJ, 881, 164